Identified particle production, azimuthal anisotropy, and interferometry measurements in Au + Au collisions at √sNN = 9.2 GeV

(STAR Collaboration) Abelev, B. I.; ...; Planinić, Mirko; ...; Poljak, Nikola; ...; Zoulkarneeva, Y.

Source / Izvornik: **Physical Review C - Nuclear Physics, 2010, 81**

Journal article, Published version
Rad u časopisu, Objavljena verzija rada (izdavačev PDF)

https://doi.org/10.1103/PhysRevC.81.024911

Permanent link / Trajna poveznica: https://urn.nsk.hr/urn:nbn:hr:217:591566

Identified particle production, azimuthal anisotropy, and interferometry measurements in Au + Au collisions at $\sqrt{s_{NN}} = 9.2$ GeV

B. I. Abelev,[8] M. M. Aggarwal,[30] Z. Ahammed,[47] A. V. Alakhverdyants,[17] B. D. Anderson,[18] D. Arkhipkin,[3] G. S. Averichev,[17] J. Balewski,[22] O. Barannikova,[8] L. S. Barnby,[2] S. Baumgart,[52] D. R. Beavis,[3] R. Bellwied,[50] F. Benedosso,[27] M. J. Betancourt,[22] R. R. Betts,[8] A. Bhasin,[16] A. K. Bhati,[30] H. Bichsel,[49] J. Bielcik,[10] J. Bielcikova,[11] B. Biritz,[6] L. C. Bland,[3] I. Bnzarov,[17] B. E. Bonner,[36] J. Bouchet,[18] E. Braidot,[27] A. V. Brandin,[25] A. Bridgeman,[1] E. Bruna,[52] S. Bueltmann,[29] T. P. Burton,[2] X. Z. Cai,[40] H. Caines,[52] M. Calderón de la Barca Sánchez,[5] O. Catu,[52] D. Cebra,[5] R. Cendejas,[6] M. C. Cervantes,[42] Z. Chajecki,[28] P. Chaloupka,[11] S. Chattopadhyay,[47] H. F. Chen,[38] J. H. Chen,[40] J. Y. Chen,[51] J. Cheng,[44] M. Cherney,[9] A. Chikanian,[52] K. E. Choi,[34] W. Christie,[3] P. Chung,[11] R. F. Clarke,[42] M. J. M. Codrington,[42] R. Corliss,[22] J. G. Cramer,[49] H. J. Crawford,[4] D. Das,[5] S. Dash,[13] L. C. De Silva,[50] R. R. Debbe,[3] T. G. Dedovich,[17] M. DePhillips,[3] A. A. Derevschikov,[32] R. Derradi de Souza,[7] L. Didenko,[3] P. Djawotho,[42] S. M. Dogra,[16] X. Dong,[21] J. L. Drachenberg,[42] J. E. Draper,[5] J. C. Dunlop,[3] M. R. Dutta Mazumdar,[47] L. G. Efimov,[17] E. Elhalhuli,[2] M. Elnimr,[50] J. Engelage,[4] G. Eppley,[36] B. Erazmus,[41] M. Estienne,[41] L. Eun,[31] P. Fachini,[3] R. Fatemi,[19] J. Fedorisin,[17] R. G. Fersch,[19] P. Filip,[17] E. Finch,[52] V. Fine,[3] Y. Fisyak,[3] C. A. Gagliardi,[42] D. R. Gangadharan,[6] M. S. Ganti,[47] E. J. Garcia-Solis,[8] A. Geromitsos,[41] F. Geurts,[36] V. Ghazikhanian,[6] P. Ghosh,[47] Y. N. Gorbunov,[9] A. Gordon,[3] O. Grebenyuk,[21] D. Grosnick,[46] B. Grube,[34] S. M. Guertin,[6] A. Gupta,[16] N. Gupta,[16] W. Guryn,[3] B. Haag,[5] T. J. Hallman,[3] A. Hamed,[42] L.-X. Han,[40] J. W. Harris,[52] J. P. Hays-Wehle,[22] M. Heinz,[52] S. Heppelmann,[31] A. Hirsch,[33] E. Hjort,[21] A. M. Hoffman,[22] G. W. Hoffmann,[43] D. J. Hofman,[8] R. S. Hollis,[8] H. Z. Huang,[6] T. J. Humanic,[28] L. Huo,[42] G. Igo,[6] A. Iordanova,[8] P. Jacobs,[21] W. W. Jacobs,[15] P. Jakl,[11] C. Jena,[13] F. Jin,[40] C. L. Jones,[22] P. G. Jones,[2] J. Joseph,[18] E. G. Judd,[4] S. Kabana,[41] K. Kajimoto,[43] K. Kang,[44] J. Kapitan,[11] K. Kauder,[8] D. Keane,[18] A. Kechechyan,[17] D. Kettler,[49] V. Yu. Khodyrev,[32] D. P. Kikola,[21] J. Kiryluk,[21] A. Kisiel,[48] S. R. Klein,[21] A. G. Knospe,[52] A. Kocoloski,[22] D. D. Koetke,[46] T. Kollegger,[12] J. Konzer,[33] M. Kopytine,[18] I. Koralt,[29] W. Korsch,[19] L. Kotchenda,[25] V. Kouchpil,[11] P. Kravtsov,[25] V. I. Kravtsov,[32] K. Krueger,[1] M. Krus,[10] L. Kumar,[30] P. Kurnadi,[6] M. A. C. Lamont,[3] J. M. Landgraf,[3] S. LaPointe,[50] J. Lauret,[3] A. Lebedev,[3] R. Lednicky,[17] C.-H. Lee,[34] J. H. Lee,[3] W. Leight,[22] M. J. LeVine,[3] C. Li,[38] N. Li,[51] Y. Li,[44] Z. Li,[51] G. Lin,[52] X. Lin,[33] S. J. Lindenbaum,[26] M. A. Lisa,[28] F. Liu,[51] H. Liu,[5] J. Liu,[36] T. Ljubicic,[3] W. J. Llope,[36] R. S. Longacre,[3] W. A. Love,[3] Y. Lu,[38] T. Ludlam,[3] G. L. Ma,[40] Y. G. Ma,[40] D. P. Mahapatra,[13] R. Majka,[52] O. I. Mall,[5] L. K. Mangotra,[16] R. Manweiler,[46] S. Margetis,[18] C. Markert,[43] H. Masui,[21] H. S. Matis,[21] Yu. A. Matulenko,[32] D. McDonald,[36] T. S. McShane,[9] A. Meschanin,[32] R. Milner,[22] N. G. Minaev,[32] S. Mioduszewski,[42] A. Mischke,[27] M. K. Mitrovski,[12] B. Mohanty,[47] D. A. Morozov,[32] M. G. Munhoz,[37] B. K. Nandi,[14] C. Nattrass,[52] T. K. Nayak,[47] J. M. Nelson,[2] P. K. Netrakanti,[33] M. J. Ng,[4] L. V. Nogach,[32] S. B. Nurushev,[32] G. Odyniec,[21] A. Ogawa,[3] H. Okada,[3] V. Okorokov,[25] D. Olson,[21] M. Pachr,[10] B. S. Page,[15] S. K. Pal,[47] Y. Pandit,[18] Y. Panebratsev,[17] T. Pawlak,[48] T. Peitzmann,[27] V. Perevoztchikov,[3] C. Perkins,[4] W. Peryt,[48] S. C. Phatak,[13] P. Pile,[3] M. Planinic,[53] M. A. Ploskon,[21] J. Pluta,[48] D. Plyku,[29] N. Poljak,[53] A. M. Poskanzer,[21] B. V. K. S. Potukuchi,[16] D. Prindle,[49] C. Pruneau,[50] N. K. Pruthi,[30] P. R. Pujahari,[14] J. Putschke,[52] R. Raniwala,[35] S. Raniwala,[35] R. L. Ray,[43] R. Redwine,[22] R. Reed,[5] J. M. Rehberg,[12] A. Ridiger,[25] H. G. Ritter,[21] J. B. Roberts,[36] O. V. Rogachevskiy,[17] J. L. Romero,[5] A. Rose,[21] C. Roy,[41] L. Ruan,[3] M. J. Russcher,[27] R. Sahoo,[41] S. Sakai,[6] I. Sakrejda,[21] T. Sakuma,[22] S. Salur,[21] J. Sandweiss,[52] J. Schambach,[43] R. P. Scharenberg,[33] N. Schmitz,[23] T. R. Schuster,[12] J. Seele,[22] J. Seger,[9] I. Selyuzhenkov,[15] P. Seyboth,[23] E. Shahaliev,[17] M. Shao,[38] M. Sharma,[50] S. S. Shi,[51] E. P. Sichtermann,[21] F. Simon,[23] R. N. Singaraju,[47] M. J. Skoby,[33] N. Smirnov,[52] P. Sorensen,[3] J. Sowinski,[15] H. M. Spinka,[1] B. Srivastava,[33] T. D. S. Stanislaus,[46] D. Staszak,[6] G. S. F. Stephans,[22] R. Stock,[12] M. Strikhanov,[25] B. Stringfellow,[33] A. A. P. Suaide,[37] M. C. Suarez,[8] N. L. Subba,[18] M. Sumbera,[11] X. M. Sun,[21] Y. Sun,[38] Z. Sun,[20] B. Surrow,[22] T. J. M. Symons,[21] A. Szanto de Toledo,[37] J. Takahashi,[7] A. H. Tang,[3] Z. Tang,[38] L. H. Tarini,[50] T. Tarnowsky,[24] D. Thein,[43] J. H. Thomas,[21] J. Tian,[40] A. R. Timmins,[50] S. Timoshenko,[25] D. Tlusty,[11] M. Tokarev,[17] T. A. Trainor,[49] V. N. Tram,[21] S. Trentalange,[6] R. E. Tribble,[42] O. D. Tsai,[6] J. Ulery,[33] T. Ullrich,[3] D. G. Underwood,[1] G. Van Buren,[3] G. van Nieuwenhuizen,[22] J. A. Vanfossen Jr.,[18] R. Varma,[14] G. M. S. Vasconcelos,[7] A. N. Vasiliev,[32] F. Videbaek,[3] Y. P. Viyogi,[47] S. Vokal,[17] S. A. Voloshin,[50] M. Wada,[43] M. Walker,[22] F. Wang,[33] G. Wang,[6] H. Wang,[24] J. S. Wang,[20] Q. Wang,[33] X. Wang,[44] X. L. Wang,[38] Y. Wang,[44] G. Webb,[19] J. C. Webb,[46] G. D. Westfall,[24] C. Whitten Jr.,[6] H. Wieman,[21] S. W. Wissink,[15] R. Witt,[45] Y. Wu,[51] W. Xie,[33] N. Xu,[21] Q. H. Xu,[39] W. Xu,[6] Y. Xu,[38] Z. Xu,[3] L. Xue,[40] Y. Yang,[20] P. Yepes,[36] K. Yip,[3] I.-K. Yoo,[34] Q. Yue,[44] M. Zawisza,[48] H. Zbroszczyk,[48] W. Zhan,[20] S. Zhang,[40] W. M. Zhang,[18] X. P. Zhang,[21] Y. Zhang,[21] Z. P. Zhang,[38] Y. Zhao,[38] C. Zhong,[40] J. Zhou,[36] W. Zhou,[39] X. Zhu,[44] Y.-H. Zhu,[40] R. Zoulkarneev,[17] and Y. Zoulkarneeva[17]

(STAR Collaboration)

[1]*Argonne National Laboratory, Argonne, Illinois 60439, USA*

[2]*University of Birmingham, Birmingham, United Kingdom*

[3]*Brookhaven National Laboratory, Upton, New York 11973, USA*

[4]*University of California, Berkeley, California 94720, USA*

[5]*University of California, Davis, California 95616, USA*

[6]*University of California, Los Angeles, California 90095, USA*

[7]*Universidade Estadual de Campinas, Sao Paulo, Brazil*

[8]*University of Illinois at Chicago, Chicago, Illinois 60607, USA*

[9] *Creighton University, Omaha, Nebraska 68178, USA*
[10] *Czech Technical University in Prague, FNSPE, Prague, CZ-11519, Czech Republic*
[11] *Nuclear Physics Institute AS CR, CZ-25068 Řež/Prague, Czech Republic*
[12] *University of Frankfurt, Frankfurt, Germany*
[13] *Institute of Physics, Bhubaneswar 751005, India*
[14] *Indian Institute of Technology, Mumbai, India*
[15] *Indiana University, Bloomington, Indiana 47408, USA*
[16] *University of Jammu, Jammu 180001, India*
[17] *Joint Institute for Nuclear Research, Dubna, RU-141980, Russia*
[18] *Kent State University, Kent, Ohio 44242, USA*
[19] *University of Kentucky, Lexington, Kentucky 40506-0055, USA*
[20] *Institute of Modern Physics, Lanzhou, People's Republic of China*
[21] *Lawrence Berkeley National Laboratory, Berkeley, California 94720, USA*
[22] *Massachusetts Institute of Technology, Cambridge, Massachusetts 02139-4307, USA*
[23] *Max-Planck-Institut für Physik, Munich, Germany*
[24] *Michigan State University, East Lansing, Michigan 48824, USA*
[25] *Moscow Engineering Physics Institute, Moscow, Russia*
[26] *City College of New York, New York, New York 10031, USA*
[27] *NIKHEF and Utrecht University, Amsterdam, The Netherlands*
[28] *Ohio State University, Columbus, Ohio 43210, USA*
[29] *Old Dominion University, Norfolk, Virginia, 23529, USA*
[30] *Panjab University, Chandigarh 160014, India*
[31] *Pennsylvania State University, University Park, Pennsylvania 16802, USA*
[32] *Institute of High Energy Physics, Protvino, Russia*
[33] *Purdue University, West Lafayette, Indiana 47907, USA*
[34] *Pusan National University, Pusan, Republic of Korea*
[35] *University of Rajasthan, Jaipur 302004, India*
[36] *Rice University, Houston, Texas 77251, USA*
[37] *Universidade de Sao Paulo, Sao Paulo, Brazil*
[38] *University of Science & Technology of China, Hefei 230026, People's Republic of China*
[39] *Shandong University, Jinan, Shandong 250100, People's Republic of China*
[40] *Shanghai Institute of Applied Physics, Shanghai 201800, People's Republic of China*
[41] *SUBATECH, Nantes, France*
[42] *Texas A&M University, College Station, Texas 77843, USA*
[43] *University of Texas, Austin, Texas 78712, USA*
[44] *Tsinghua University, Beijing 100084, People's Republic of China*
[45] *United States Naval Academy, Annapolis, Maryland 21402, USA*
[46] *Valparaiso University, Valparaiso, Indiana 46383, USA*
[47] *Variable Energy Cyclotron Centre, Kolkata 700064, India*
[48] *Warsaw University of Technology, Warsaw, Poland*
[49] *University of Washington, Seattle, Washington 98195, USA*
[50] *Wayne State University, Detroit, Michigan 48201, USA*
[51] *Institute of Particle Physics, CCNU (HZNU), Wuhan 430079, People's Republic of China*
[52] *Yale University, New Haven, Connecticut 06520, USA*
[53] *University of Zagreb, Zagreb, HR-10002, Croatia*

(Received 23 September 2009; published 26 February 2010)

We present the first measurements of identified hadron production, azimuthal anisotropy, and pion interferometry from Au + Au collisions below the nominal injection energy at the BNL Relativistic Heavy-Ion Collider (RHIC) facility. The data were collected using the large acceptance solenoidal tracker at RHIC (STAR) detector at $\sqrt{s_{NN}} = 9.2$ GeV from a test run of the collider in the year 2008. Midrapidity results on multiplicity density dN/dy in rapidity y, average transverse momentum $\langle p_T \rangle$, particle ratios, elliptic flow, and Hanbury-Brown–Twiss (HBT) radii are consistent with the corresponding results at similar $\sqrt{s_{NN}}$ from fixed-target experiments. Directed flow measurements are presented for both midrapidity and forward-rapidity regions. Furthermore the collision centrality dependence of identified particle dN/dy, $\langle p_T \rangle$, and particle ratios are discussed. These results also demonstrate that the capabilities of the STAR detector, although optimized for $\sqrt{s_{NN}} = 200$ GeV, are suitable for the proposed QCD critical-point search and exploration of the QCD phase diagram at RHIC.

DOI: 10.1103/PhysRevC.81.024911 PACS number(s): 25.75.Dw, 24.85.+p, 25.75.Gz, 25.75.Ld

I. INTRODUCTION

Exploring the quantum chromodynamics phase diagram is one of the goals of high-energy heavy-ion collision experiments [1]. The QCD phase diagram is usually plotted as temperature T versus baryon chemical potential μ_B. Assuming a thermalized system is reached in heavy-ion collisions, both of these quantities can be varied by changing the collision energy [2]. The phase diagram shows a possible transition from a high-energy-density and high-temperature phase dominated by partonic degrees of freedom, to a phase where the relevant degrees of freedom are hadronic [3]. Several observations at the top RHIC energy, such as the suppression of high transverse momentum p_T hadron production in Au + Au collisions relative to $p + p$ collisions [4], large elliptic flow v_2 for hadrons with light, as well as heavier strange valence quarks, and differences between baryon and meson v_2 at intermediate p_T for Au + Au collisions, have been associated with the existence of a phase with partonic degrees of freedom in the initial stages of heavy-ion collisions [1,4,5]. Lowering the collision energy and studying the energy dependence of these observables will allow us to search as a function of center-of-mass energy $\sqrt{s_{NN}}$ or (T, μ_B) for the onset of the transition to a phase with partonic degrees of freedom at the early stage of the collision.

Lattice QCD calculations indicate that the system produced at $\mu_B = 0$ evolves through a rapid crossover in the quark-hadron phase transition [6]. Calculations from lattice QCD [7] and those from several QCD-based models [8] suggest that for collisions corresponding to large μ_B, the transition is first order. The point in the (T,μ_B) plane where the first-order phase transition ends, is the QCD critical point [9]. Theoretical predictions of the location of this point on the phase diagram are subject to various ambiguities [10]. An experimental program for locating the QCD critical point through its signatures [10,11] (e.g., long-range fluctuations in event-by-event observables) is one of the exciting possibilities at the RHIC facility. These motivations form the basis of the proposal [12] by the experiments at RHIC to carry out a detailed program of exploring the phase diagram by varying the collision energy in high-energy heavy-ion collisions.

As an initial step to test the capabilities of the collider and experiments, a short run was conducted in the year 2008 at RHIC. The Au ions were collided at $\sqrt{s_{NN}} = 9.2$ GeV, which is below the injection energy of $\sqrt{s_{NN}} = 19.6$ GeV. At and below nominal injection energy, RHIC runs as a colliding storage ring, further details of which can be found in Ref. [13]. The data-taking period lasted for less than 5 h at the solenoidal tracker at RHIC (STAR) experiment. This paper presents results based on the analysis of this small data set and demonstrates the success of the test run in achieving its objectives. The measurements shown here are the first step toward a detailed exploration of the QCD phase diagram at RHIC.

The paper is organized as follows. The next section briefly presents the detectors used and details of the data analysis. In Sec. III, we present the results including p_T spectra, dN/dy, $\langle p_T \rangle$, and particle ratios as a function of collision centrality and $\sqrt{s_{NN}}$. We also discuss results on directed flow v_1, elliptic flow v_2, and pion interferometry in this section. In Sec. IV, we discuss the freeze-out conditions. Finally, in Sec. V we summarize the results and provide a brief outlook for the upcoming beam energy scan program at RHIC.

II. EXPERIMENT AND DATA ANALYSIS

A. STAR detector

The results presented here are based on data taken at STAR [14] in Au + Au collisions at $\sqrt{s_{NN}} = 9.2$ GeV. This data set is taken with a minimum-bias trigger. The trigger detectors used are the beam-beam counter (BBC) and vertex position detector (VPD) [15]. The BBCs are scintillator annuli mounted around the beam pipe beyond the east and west pole-tips of the STAR magnet at about 375 cm from the center of the nominal interaction region (IR). The inner tiles of the BBCs, with a pseudorapidity η range of $3.8 < |\eta| < 5.2$ and full azimuthal coverage $\Delta\phi = 2\pi$, are used to reconstruct the first-order event plane for the directed flow analysis. The VPDs are based on the conventional technology of plastic scintillator readout by photomultiplier tubes. They consist of two identical detector assemblies very close to the beam pipe, one on each side at a distance of $|V_z| = 5.6$ m from the center of the IR. The main detector used to obtain the results on p_{T} spectra, yields, particle ratios, azimuthal anisotropy parameters, and pion interferometry for charged hadrons is the time projection chamber (TPC) [16]. The TPC is the primary tracking device at STAR. It is 4.2 m long and 4 m in diameter. Its acceptance covers ± 1.8 units of pseudorapidity η and the full azimuthal angle. The sensitive volume of the TPC contains P10 gas (10% methane, 90% argon) regulated at 2 mbar above atmospheric pressure. The TPC data are used to determine particle trajectories, momenta, and particle type through ionization energy loss (dE/dx). STAR's solenoidal magnet field used for this low-energy Au + Au test run was 0.5 T.

In addition we present directed flow measurements from forward rapidities. These results used the data taken by the forward time projection chambers (FTPCs) [17]. There are two FTPCs located around the beam axis on both sides of the collision point. The sensitive medium is a gas mixture of equal parts Ar and CO_2 by weight. The FTPCs detect charged particles in the pseudorapidity region $2.5 \leqslant |\eta| \leqslant 4.0$, with full azimuthal coverage. The details of the design and other characteristics of the STAR detectors can be found in Ref. [14].

B. Event selection

The primary vertex for each minimum-bias event is determined by finding the best point of common origin of the tracks measured in the TPC. The distribution of the primary vertex position along the longitudinal beam direction V_z is shown in

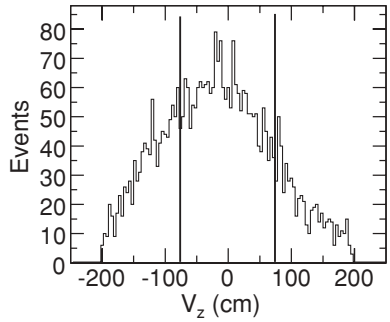

FIG. 1. Event-by-event distribution of the z position of the primary vertex V_z in Au + Au collisions at $\sqrt{s_{NN}} = 9.2$ GeV. The vertical solid lines show the condition of $|V_z| < 75$ cm for selected events.

Fig. 1. The distribution is a broad Gaussian varying between −200 and 200 cm, with a root-mean-square deviation of 89 cm. Only those events which have a V_z within 75 cm of the nominal collision point (center of the detector) are selected for the analysis, corresponding to 57% of the total events recorded. This value is chosen by the tradeoff between uniform detector performance within $|\eta| < 1.0$ and sufficient statistical significance of the measured observables. To reject events which involve interactions with the beam pipe and beam-gas interactions, the event vertex radius (defined as $\sqrt{V_x^2 + V_y^2}$, where V_x and V_y are the vertex positions along the x and y directions) is required to be less than 2 cm. The V_x vs V_y distribution is shown in Fig. 2. The circle with dotted lines corresponds to the event vertex radius of 2 cm. A total of about 3000 events pass the selection criteria described above.

C. Centrality selection

Centrality classes in Au + Au collisions at $\sqrt{s_{NN}} =$ 9.2 GeV are defined using the number of charged-particle tracks reconstructed in the main TPC over the full azimuth, pseudorapidity $|\eta| < 0.5$ and $|V_z| < 75$ cm.

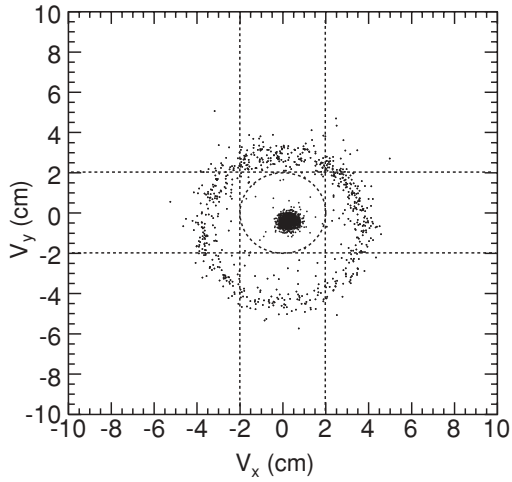

FIG. 2. Event-by-event distribution of V_x vs V_y in Au + Au collisions at $\sqrt{s_{NN}} = 9.2$ GeV. The circle with dotted lines corresponds to a radius ($=\sqrt{V_x^2 + V_y^2}$) of 2 cm.

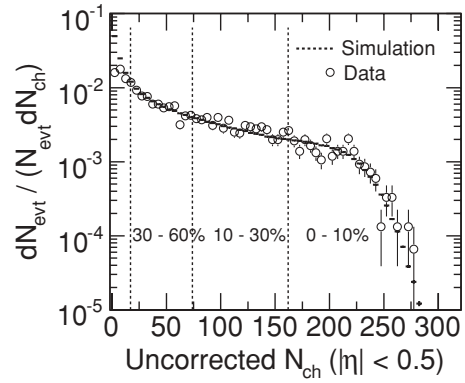

FIG. 3. Uncorrected charged-particle multiplicity distribution (open circles) measured in the TPC within $|\eta| < 0.5$ in Au + Au collisions at $\sqrt{s_{NN}} = 9.2$ GeV. The dashed histogram represents the simulated multiplicity distribution. The vertical dashed lines reflect the centrality selection criteria used in the paper. Errors are statistical only.

Figure 3 shows the uncorrected multiplicity distribution for charged tracks from the real data ($N_{\rm ch}^{\rm TPC}$, open circles) and for those obtained from simulation (dashed histogram). Simulated multiplicity density is calculated using the two-component model [18] with the number of participants $N_{\rm part}$ and number of collisions $N_{\rm coll}$ extracted from the Glauber Monte Carlo simulation as

$$\frac{dN_{\rm ch}}{d\eta} = n_{pp}\left[(1-x)\frac{N_{\rm part}}{2} + xN_{\rm coll}\right]. \qquad (1)$$

Here n_{pp} is the average multiplicity in minimum-bias $p + p$ collisions and x is the fraction of the hard component. The inelastic cross section for $p + p$ collisions used in the Glauber model simulations is 31.5 mb [19]. The event-by-event multiplicity fluctuation has been taken into account by convoluting the negative binomial distributions (NBDs) for a given $N_{\rm part}$ and $N_{\rm coll}$. The NBD distribution in multiplicity n has two parameters, n_{pp} and k, and is defined as

$$P_{\rm NBD}(n_{pp}, k; n) = \frac{\Gamma(n+k)}{\Gamma(n+1)\Gamma(k)}\frac{(n_{pp}/k)^n}{(n_{pp}/k+1)^{n+k}}, \qquad (2)$$

where Γ is the gamma function. The values $k = 2.1$ and $n_{pp} = 1.12$ are obtained by fitting the measured multiplicities with those from the simulation. The simulated multiplicity distribution is not sensitive to the k parameter. The distributions are found to be similar for varying k values such as $k =$ 1.0, 1.6, and 3.0. The fitting is performed for $N_{\rm ch} > 17$ in order to avoid the trigger inefficiency in peripheral collisions. The x value is fixed at 0.11 ± 0.03, obtained by extrapolating data obtained from the PHOBOS Collaboration [20]. The centrality is defined by calculating the fraction of the total cross section obtained from the simulated multiplicity.

Table I lists the centrality selection criteria for Au + Au collisions at $\sqrt{s_{NN}} = 9.2$ GeV. We have divided the events into three centrality classes, 0–10%, 10–30%, and 30–60% of the total cross section. The mean values of $N_{\rm part}$ and $N_{\rm coll}$ have been evaluated for these centrality bins and are given in

TABLE I. Centrality selection, average number of participating nucleons $\langle N_{\rm part}\rangle$, and average number of binary collisions $\langle N_{\rm coll}\rangle$.

% cross section	$N_{\rm ch}^{\rm TPC}$	$\langle N_{\rm part}\rangle$	$\langle N_{\rm coll}\rangle$
0–10	>162	317 ± 4	716 ± 83
10–30	74–162	202 ± 11	395 ± 34
30–60	17–74	88 ± 10	133 ± 20

Table I. Systematic uncertainties on $\langle N_{\rm part}\rangle$ and $\langle N_{\rm coll}\rangle$ have been estimated by varying n_{pp} and x in the two-component model as well as varying the input parameters in the Glauber Monte Carlo simulation. The final errors on $\langle N_{\rm part}\rangle$ and $\langle N_{\rm coll}\rangle$ are the quadrature sum of these individual systematic errors. The results presented in this paper cover the collision centrality range of 0–60%. The results from more peripheral collisions are not presented due to large trigger inefficiencies in this test run.

D. Track selection and particle identification

Track selection criteria for the various analyses are presented in Table II. To avoid admixture of tracks from secondary vertices, a requirement is placed on the distance of closest approach (DCA) between each track and the event vertex. To prevent multiple counting of split tracks, a condition is placed on the number of track points ($N_{\rm fit}$) used in the reconstruction of the track. Tracks can have a maximum of 45 hits in the TPC.

To extract the pion yield in a given p_T bin, we perform an eight-Gaussian fit to the normalized dE/dx distributions of positively charged and negatively charged hadrons, simultaneously. The normalized dE/dx in general is defined as

$$n\sigma_X = \frac{\log[(dE/dx)/B_X]}{\sigma_X}, \tag{3}$$

where X is the particle type ($e^{\pm}$, $\pi^{\pm}$, $K^{\pm}$, p, or $\bar{p}$), B_X is the expected mean dE/dx of particle X, and σ_X is the dE/dx resolution of the TPC, which is a function of the track length in the TPC. The expected mean dE/dx of particle X is calculated using a Bichsel function for the energy loss in thin layers of P10 in the STAR TPC [16,21]. Good agreement between the measurement and the calculation was demonstrated previously [22]. Figure 4 shows a typical dE/dx distribution normalized to the pion dE/dx (referred to as the $n\sigma_\pi$ distribution) for charged hadrons with $0.3 < p_T < 0.4$ GeV/c and $|y| < 0.5$. The counts under the Gaussian about $n\sigma_\pi \sim 0$ give the yield of

TABLE II. Track selection criteria for various analyses presented in this paper.

Analysis	DCA (cm)	$N_{\rm fit}$	η or y	p_T (GeV/c)
p_T spectra	<3	>20	$\lvert y\rvert < 0.5$	>0.1
v_1(TPC)	<1	>20	$\lvert\eta\rvert < 1.3$	0.15–2.0
v_1(FTPC)	<1	>5	$2.5 < \lvert\eta\rvert < 4.0$	0.15–2.0
v_2	<3	>15	$\lvert\eta\rvert < 1.0$	0.1–2.0
HBT	<3	>15	$\lvert y\rvert < 0.5$	k_T : 0.15–0.25

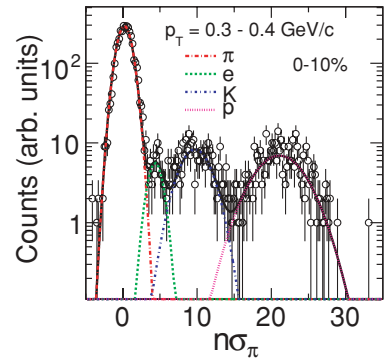

FIG. 4. (Color online) dE/dx distribution for positively charged hadrons in the TPC, normalized by the expected pion dE/dx at $0.3 < p_T < 0.4$ GeV/c and $|y| < 0.5$ in Au + Au collisions at $\sqrt{s_{NN}} = 9.2$ GeV. The curves are Gaussian fits representing contributions from pions (dot-dashed, red), electrons (dashed, green), kaons (dot-dashed, blue), and protons (dotted, magenta). See text for details. Errors are statistical only.

pions for a particular p_T range. A similar procedure is followed to obtain yields for other p_T ranges and for yields of kaons and protons. Further details of extracting raw yields of identified hadrons from normalized dE/dx distributions can be found in Ref. [23].

For the elliptic flow analysis of identified hadrons, the criteria of $|n\sigma_\pi| < 2$ and $|n\sigma_p| < 2$ are used for extracting pion and proton v_2. Since the measurements are carried out at low p_T (<1.0 GeV/c), such an identification criterion is reasonable. For the pion interferometry analysis, the particle identification conditions are $|n\sigma_\pi| < 2$, $|n\sigma_p| > 2$, and $|n\sigma_K| > 2$, and the average transverse momentum, $k_T = (|\vec{p}_{1\rm T} + \vec{p}_{2\rm T}|)/2$, is required to fall in the range 150–250 MeV/c.

E. Event plane for azimuthal anisotropy

Azimuthal anisotropy can be quantified by studying the Fourier expansion of the azimuthal angle ϕ distribution of produced particles with respect to the reaction plane angle Ψ_R [24]. The various (order n) coefficients in this expansion are defined as

$$v_n = \langle\cos[n(\phi - \Psi_R)]\rangle. \tag{4}$$

The angular brackets in the definition denote an average over many particles and events. Directed flow can be quantified by the first coefficient v_1 and elliptic flow by the second coefficient v_2, obtained using the above equation.

In the azimuthal anisotropy analysis, v_1 and v_2 are obtained from the following procedure. The event flow vector Q_n and the event plane angle Ψ_n are defined by [24]

$$Q_n\cos(n\Psi_n) = Q_{nx} = \sum_i w_i\cos(n\phi_i), \tag{5}$$

$$Q_n\sin(n\Psi_n) = Q_{ny} = \sum_i w_i\sin(n\phi_i), \tag{6}$$

$$\Psi_n = \left(\tan^{-1}\frac{Q_{ny}}{Q_{nx}}\right)\Big/ n, \tag{7}$$

where sums go over all particles i used in the event plane calculation, and ϕ_i and w_i are the laboratory azimuthal angle and the weight for the ith particle, respectively. Tracks used for the calculation of v_n are excluded from the calculation of the event plane to remove self-correlation effects.

Since finite multiplicity limits the angular resolution of the reaction plane reconstruction, the $v_n^{\rm obs}$ has to be corrected for the event plane resolution by

$$v_n = \frac{v_n^{\rm obs}}{\langle \cos[n(\Psi_n - \Psi_R)]\rangle} \tag{8}$$

to obtain the real v_n, where angular brackets denote an average over a large event sample. The event plane resolution is estimated from the correlation of the event planes of two subevents. Assuming the pure flow correlations between the subevents, the event plane resolution is given by

$$\left\langle \cos\left[n\left(\Psi_n^A - \Psi_R\right)\right]\right\rangle = \sqrt{\left\langle \cos\left[n\left(\Psi_n^A - \Psi_n^B\right)\right]\right\rangle}, \tag{9}$$

where A and B denote two subgroups of tracks. In this analysis, we use two random subevents with equal numbers of particles. The full event plane resolution is obtained from the resolution of the subevents by

$$\langle \cos[n(\Psi_n - \Psi_R)]\rangle = C\left\langle \cos\left[n\left(\Psi_n^A - \Psi_R\right)\right]\right\rangle, \tag{10}$$

where C is a constant calculated from the known dependence of the resolution on multiplicity [24].

For the elliptic flow measurements presented in this paper, the TPC tracks are used to reconstruct the reaction plane [24]. The weights are taken to be the value of p_T in GeV/c up to 2 GeV/c and then constant at 2.0 for $p_T > 2$ GeV/c. Such weight values are chosen as v_2 increases with p_T up to 2 GeV/c and then tends to saturates beyond $p_T = 2$ GeV/c. The variation of event plane resolution with collision centrality is shown in Fig. 5. The values of the resolution depend on the multiplicity and flow observed in the events. The resolution values are lower for $\sqrt{s_{NN}} = 9.2$ GeV, compared to collisions at $\sqrt{s_{NN}} = 200$ GeV for similarly defined collision centrality classes [25]. A similar procedure for correcting the observed flow values with the resolution factor is followed for v_1 measurements. The v_1 results presented here are obtained using two different methods: the mixed harmonics and the standard methods.

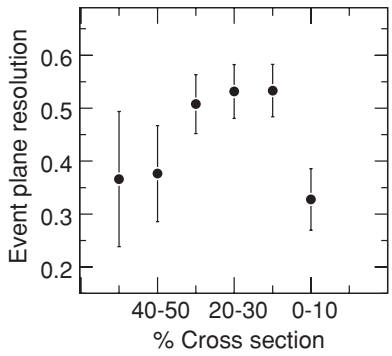

FIG. 5. Second-order event plane resolution measured in the TPC as a function of collision centrality for Au + Au collisions at $\sqrt{s_{NN}} = 9.2$ GeV. Errors are statistical only.

In the mixed harmonics method, v_1 is calculated using mixed harmonics involving the second-harmonic event plane [25]. This method utilizes the large elliptic flow signal and at the same time suppresses the nonflow contributions arising from the correlation of particles from the same harmonics. The method uses the second-order event plane from the TPC ($\Psi_2^{\rm TPC}$) and the first-order event plane from random subevents in the FTPCs ($\Psi_1^{\rm FTPC1}$ and $\Psi_1^{\rm FTPC2}$). The average resolution for the event plane [as defined in Eqs. (9) and (10)] reconstructed from the TPC is 0.46 ± 0.03, while that reconstructed from the FTPCs is 0.41 ± 0.03, for 0–60% collision centrality. The mixed harmonics method is denoted by $v_1\{\mathrm{EP}_1, \mathrm{EP}_2\}$ [25], as given below:

$$v_1\{\mathrm{EP}_1, \mathrm{EP}_2\} = \frac{\left\langle \cos\left(\phi + \Psi_1^{\rm FTPC} - 2\Psi_2^{\rm TPC}\right)\right\rangle}{\sqrt{\left\langle \cos\left(\Psi_1^{\rm FTPC1} + \Psi_1^{\rm FTPC2} - 2\Psi_2^{\rm TPC}\right)\right\rangle \mathrm{Res}\left(\Psi_2^{\rm TPC}\right)}}, \tag{11}$$

where the emission angle of the particle (ϕ) is correlated with the $\Psi_1^{\rm FTPC}$ of the random subevent composed of tracks from both the FTPCs excluding that particle.

In the standard method, the first-order event plane is reconstructed separately from the FTPC tracks ($v_1\{\mathrm{EP}_1, \mathrm{FTPC}\}$) and from the BBC hits ($v_1\{\mathrm{EP}_1, \mathrm{BBC}\}$). The event plane reconstructed from the detector on one side of the collision (east or west) is called a subevent plane. A combination of the east and west subevent plane vectors provides the full event plane. In the $v_1\{\mathrm{EP}_1, \mathrm{FTPC}\}$ method, we used the event plane obtained from the full FTPC region to obtain the directed flow values measured in the TPC range ($|\eta| < 1.3$). A self-correlation arises if v_1 is obtained using particles from the same pseudorapidity region as is used for the event plane reconstruction. To avoid this self-correlation in the $v_1\{\mathrm{EP}_1, \mathrm{FTPC}\}$ method, v_1 is obtained in the east FTPC ($-4.2 < \eta < -2.5$) by using the event plane reconstructed in the west FTPC ($2.5 < \eta < 4.2$), and *vice versa*. In the $v_1\{\mathrm{EP}_1, \mathrm{BBC}\}$ method, the event plane is obtained from the full BBC region ($3.8 < |\eta| < 5.2$). Particles used for the estimation of v_1 with respect to the BBC full event plane cover the η range up to 3.8, in order to avoid the self-correlation. The average resolution of the first-order event plane for $v_1\{\mathrm{EP}_1, \mathrm{FTPC}\}$ is 0.41 ± 0.03 for 0–60% central collisions, while that for $v_1\{\mathrm{EP}_1, \mathrm{BBC}\}$ is 0.24 ± 0.07.

F. Correlation function in π interferometry

Experimentally, the two-particle correlation function is obtained from the ratio

$$C(\vec{q}, \vec{k}) = \frac{A(\vec{q}, \vec{k})}{B(\vec{q}, \vec{k})}, \tag{12}$$

where $A(\vec{q}, \vec{k})$ is the distribution of particle pairs with relative momentum $\vec{q} = \vec{p}_1 - \vec{p}_2$ and average momentum $\vec{k} = (\vec{p}_1 + \vec{p}_2)/2$ from the same event, and $B(\vec{q}, \vec{k})$ is the corresponding distribution for pairs of particles taken from different events [26,27]. The correlation function is normalized to unity at large

$\vec{q}$. In the mixed events, each particle in a given event is mixed with all particles (π^- for the results presented in this paper) from other events, within a collection of 50 similar events. Similar events are selected within the centrality bin and further binned to have primary vertex z positions within 10 cm. With the availability of high-statistics data and development of new techniques, it has become possible to have a three-dimensional decomposition of $\vec{q}$ [28–30], providing better insight into the collision geometry.

The relative momentum $\vec{q}$ can be decomposed according to the Bertsch-Pratt (also known as "out-side-long") convention [31]. The relative momentum $\vec{q}$ is decomposed into the variables along the beam direction ($q_{\rm long}$), parallel ($q_{\rm out}$) to the transverse momentum of the pair $\vec{k}_T = (\vec{p}_{1T} + \vec{p}_{2T})/2$, and perpendicular ($q_{\rm side}$) to $q_{\rm long}$ and $q_{\rm out}$. In addition to the correlation arising from quantum statistics of two identical particles, correlations can also arise from two-particle final-state interactions. For identical pions, the effects of strong interactions are negligible, but the long-range Coulomb repulsion causes a suppression of the measured correlation function at small $\vec{q}$.

In this analysis, we follow the same procedure as was used in the previous analysis of Au + Au collisions at $\sqrt{s_{NN}} =$ 200 GeV [32]. For an azimuthally integrated analysis at midrapidity in the longitudinal co-moving system (LCMS), the correlation function in Eq. (12) can be decomposed as [33]

$$C(q_{\rm out}, q_{\rm side}, q_{\rm long}) = (1-\lambda) + \lambda K_{\rm coul}(q_{\rm inv})\left(1 + e^{-q_{\rm out}^2 R_{\rm out}^2 - q_{\rm side}^2 R_{\rm side}^2 - q_{\rm long}^2 R_{\rm long}^2}\right), \quad (13)$$

where $K_{\rm coul}$ is to a good approximation the squared nonsymmetrized Coulomb wave function integrated over a Gaussian source (corresponding to the LCMS Gaussian radii $R_{\rm out}$, $R_{\rm side}$, $R_{\rm long}$) [34]. Assuming particle identification is perfect and the source is purely chaotic, λ represents the fraction of correlated pairs emitted from the collision.

We assume a spherical Gaussian source of 5 fm [31,32] for Au + Au collisions at $\sqrt{s_{NN}} = 9.2$ GeV. The first term $(1-\lambda)$ in Eq. (13) accounts for those pairs which do not interact or interfere. The second term represents those pairs where both Bose-Einstein effects and Coulomb interactions are present [32].

G. Correction factors for p_T spectra

Two major correction factors for p_T spectra account for the detector acceptance and for the efficiency of reconstructing particle tracks. These are determined together by embedding the tracks simulated using the GEANT [35] model of the STAR detector into real events at the raw data level. One important requirement is to have a match in the distributions of reconstructed embedded tracks and real data tracks for quantities reflecting track quality and used for track selection. Figures 6(a) and 6(b) show the comparisons of DCA (for protons) and $N_{\rm fit}$ (for pions) distributions, respectively, in the range $0.4 < p_T < 0.7$ GeV/c. Similar agreement as in Fig. 6 is observed between embedded tracks and real data in other

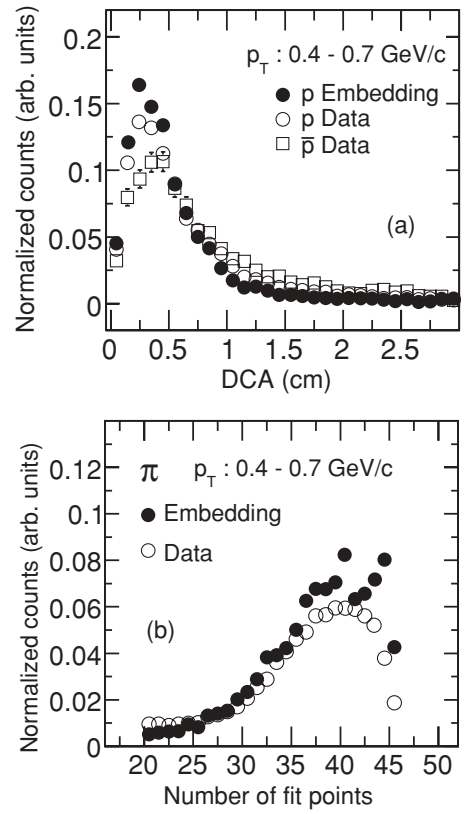

FIG. 6. (a) Distribution of distance of closest approach of proton tracks to the primary vertex. The embedded tracks are compared with the ones in real data at $0.4 < p_T < 0.7$ GeV/c at midrapidity in Au + Au collisions at $\sqrt{s_{NN}} = 9.2$ GeV. The DCA distribution of antiprotons in a similar kinematic range is also shown for comparison. (b) Comparison between the distributions of number of fit points for pions from embedding and from real data for $0.4 < p_T < 0.7$ GeV/c at midrapidity in Au + Au collisions at $\sqrt{s_{NN}} = 9.2$ GeV.

measured p_T ranges for all the identified hadrons presented in this paper. The ratio of the distribution of reconstructed and original Monte Carlo tracks as a function of p_T gives the acceptance × efficiency correction factor as a function of p_T for the rapidity interval studied. The typical efficiency × acceptance factors in 0–60% central collisions for pions, kaons, and protons at midrapidity ($|y| < 0.5$) are shown in Fig. 7(a). The raw yields are corrected by these factors to obtain the final p_T spectra.

The STAR experiment previously observed that proton yields had significant contamination from secondary protons, due to the interactions of energetic particles produced in collisions with detector materials. As these secondary protons are produced away from the primary interaction point, they appear as a long tail in the DCA distribution of protons. A comparison between shapes of DCA distributions of protons and antiprotons (which do not have such sources of background) was used in the STAR experiment to estimate the background contribution to the proton yield [23,36]. This feature was found to be more pronounced at lower p_T. In this test run, it is observed that the DCA distribution for protons does not exhibit a long tail, and that for all the p_T ranges studied, its shape is similar to that for antiprotons [Fig. 6(a), distributions

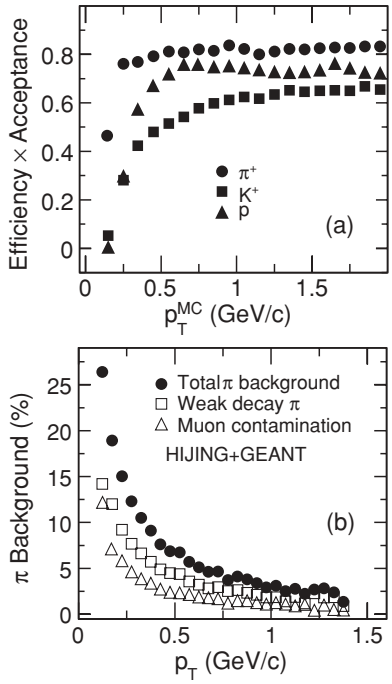

FIG. 7. (a) Efficiency × acceptance for reconstructed pions, kaons, and protons in the TPC as a function of p_T at midrapidity in Au + Au collisions at $\sqrt{s_{NN}} = 9.2$ GeV. (b) Percentage of pion background contribution estimated from HIJING + GEANT as a function of p_T at midrapidity in Au + Au collisions at $\sqrt{s_{NN}} =$ 9.2 GeV. The contributions from different sources and the total background are shown separately.

normalized to the same number of total counts]. This lack of secondary protons for Au + Au collisions at $\sqrt{s_{NN}} = 9.2$ GeV could be due to the experimental configuration in the year 2008 with reduced amount of material in front of the STAR TPC, and due to the relatively small number of energetic particles produced in the interactions compared to collisions at higher energies of $\sqrt{s_{NN}} = 62.4$ and 200 GeV. No corrections for secondary proton background are applied in the present analysis at $\sqrt{s_{NN}} = 9.2$ GeV.

The charged-pion spectra are corrected for feed-down from weak decays, muon contamination, and background pions produced in the detector materials. These corrections are obtained from Monte Carlo simulations of HIJING events at $\sqrt{s_{NN}} = 9.2$ GeV, with the STAR geometry for year 2008 and a realistic description of the detector response used in GEANT. The simulated events are reconstructed in the same way as the real data. The weak-decay daughter pions are mainly from K^0_S and are identified by the parent particle information accessible from the simulation. The muons from pion decay can be misidentified as primordial pions due to their similar masses. This contamination is obtained from Monte Carlo simulations by identifying the decay, which is accessible in the simulation. The weak-decay pion background and muon contamination obtained from the simulation are shown in Fig. 7(b), as a function of simulated pion p_T for 0–60% central Au + Au collisions at $\sqrt{s_{NN}} = 9.2$ GeV. The final pion spectra are corrected for this background effect.

The low-momentum particles lose energy while traversing the detector material. The track reconstruction algorithm takes into account the Coulomb scattering and energy loss, assuming the pion mass for each particle. Therefore, a correction for the energy loss by heavier particles ($K^{\pm}$, p, and $\bar{p}$) is needed. This correction is obtained from embedding Monte Carlo simulations. The largest change in reconstructed p_T is found to be ~20 MeV/c at $p_T = 200$ MeV/c. For all results presented in this paper, the track p_T is corrected for this energy loss effect.

H. Systematic errors

Systematic uncertainties on the spectra are estimated by varying cuts and by assessing the purity of identified hadron sample from dE/dx measurements. In addition, the Gaussian fit ranges are varied to estimate the systematic uncertainty on the extracted raw spectra. The point-to-point systematic errors are quoted in figure captions. The statistical and systematic errors are added in quadrature and plotted for most of the results unless otherwise specified. For integrated particle yields, extrapolating yields to unmeasured regions in p_T is an additional source of systematic error. These are estimated by comparing the extrapolations using different fit functions to the p_T spectra. The detailed procedure is described in Ref. [23]. A summary of various sources of systematic errors on the identified hadron yields for 0–60% centrality in Au + Au collisions at $\sqrt{s_{NN}} = 9.2$ GeV is given in Table III. The column titled "V_z" in Table III represents the systematic errors obtained by varying the V_z range in the analysis, "Cuts" lists systematic errors due to variation of DCA and N_{fit} cut values, "y" represents the systematic effect on yields due to a variation in rapidity range from ±0.5 to ±0.2, "Corr." includes the contribution to systematic errors from track reconstruction efficiency and acceptance estimates, "PID" represents the systematic errors associated with particle identification (obtained by varying the dE/dx cuts and the range of Gaussian fits to normalized dE/dx distributions), and "Extrapol." refers to the contribution of systematic errors from the different fit functions used for obtaining yields in unmeasured p_T ranges. In addition, the systematic error arising due to the pion background estimation (discussed in the previous subsection) is also calculated. It is of the order of 6%. The total systematic errors are of the order of 11%, 16%, and 20% for pion, kaon, and proton yields, respectively.

The systematic errors in the directed flow analysis are obtained by (a) exploiting the symmetry in the measurements for forward and backward regions with respect to $\eta = 0$, and (b) comparing v_1 calculated from different methods with

TABLE III. Sources of systematic errors on yields of various produced hadrons. See Sec. II H for more details.

Hadron	V_z	Cuts	y	Corr.	PID	Extrapol.
π	3%	3.2%	2%	5%	5%	3%
K	3%	6.2%	2%	5%	10%	8%
p	3%	5.4%	10%	5%	4%	15%

various sensitivities to nonflow effects [25]. In (a), we average v_1 from the mixed harmonics method ($v_1\{EP_1, EP_2\}$) and from the two standard methods ($v_1\{EP_1, FTPC\}$ and $v_1\{EP_1, BBC\}$), as discussed in Sec. II E, and take the difference between the magnitude of v_1 in the forward and backward region as the systematic error due to the unbalanced detector response. We report an absolute error of ∼7.8% in the FTPC range ($2.5 < |\eta| < 4.2$), and negligible error in the TPC range. In (b), we average the magnitude of v_1 in the forward and backward region, and take the maximum difference between results from the three methods as the systematic uncertainty. An absolute error of ∼10% is found for the FTPC range, and ∼50% relative error for the TPC range. The $v_1\{EP_1, BBC\}$ method in the TPC range ($|\eta| < 1.3$) is more reliable than the other two methods. This is due to the large η gap between the BBC and TPC detectors, which helps subtract the nonflow effect. The η gap between the BBC and the TPC is up to 2.6 units, while it is only 1.3 units between the FTPC and the TPC. The total absolute systematic error on the v_1 estimate is calculated as the quadrature sum of components (a) and (b), which is ∼10% (absolute error) for the FTPC range and ∼50% (relative value) for the TPC range.

The systematic errors on the elliptic flow parameter are evaluated by varying the event vertex selection along the beam direction, varying the DCA cut value, and by using the η subevent method. The total systematic error on v_2 is approximately 10%.

For the pion interferometry analysis, we study the following sources of systematic error: track merging, track splitting, size of the source used for Coulomb correction, particle identification, and pair acceptance for pions of opposite charges. The estimated systematic errors are less than 10% for all radii in the 0–60% centrality bin for $150 < k_T < 250$ MeV/c, similar to those in Refs. [31,32].

III. RESULTS

A. Transverse momentum spectra

Figures 8(a) and 8(b) show the transverse momentum spectra for $\pi^{\pm}$ and p ($\bar{p}$), respectively. Figures 9(a) and 9(b) show the spectra for K^+ and K^-, respectively, in Au + Au collisions at $\sqrt{s_{NN}} = 9.2$ GeV. The results are shown for the collision centrality classes of 0–10%, 10–30%, 30–60%, and 0–60%. The $\bar{p}$ spectrum is shown only for 0–60% centrality, and the yields are multiplied by a factor of 10 for visibility. The inverse slopes of the identified hadron spectra follow the order $\pi < K < p$. An exponential fit to the p_T spectra of π^+, K^+, and p yields inverse slopes of 180 ± 7, 360 ± 7, and 616 ± 11 MeV, respectively. The errors on the inverse slopes are statistical. The spectra can be further characterized by looking at the dN/dy and $\langle p_T \rangle$ or $\langle m_T \rangle - m$ for the produced hadrons, where m is the mass of the hadron and $m_T = \sqrt{m^2 + p_T^2}$ is its transverse mass. Those observables are discussed in the following sections.

B. Centrality dependence of particle production

Figures 10 and 11 show the comparison of collision centrality dependence of dN/dy of π^+, $K^{\pm}$, and p, normalized

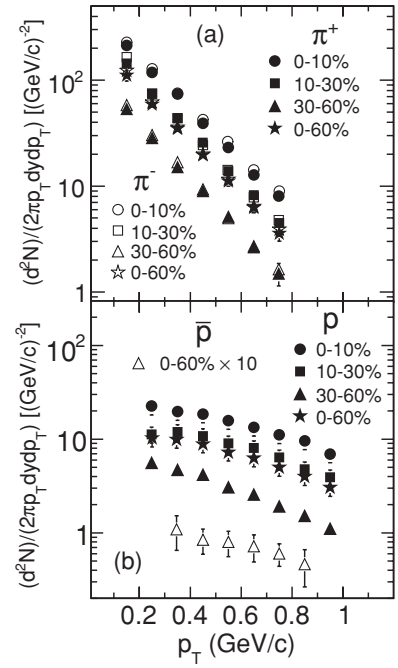

FIG. 8. Transverse momentum spectra for (a) charged pions and (b) protons at midrapidity ($|y| < 0.5$) in Au + Au collisions at $\sqrt{s_{NN}} = 9.2$ GeV for various centralities. The distributions for antiprotons were measured in this limited statistics data only for 0–60% centrality. The antiproton yield shown in the figure is multiplied by a factor of 10. The errors shown are statistical and systematic errors (discussed in Sec. II H) added in quadrature.

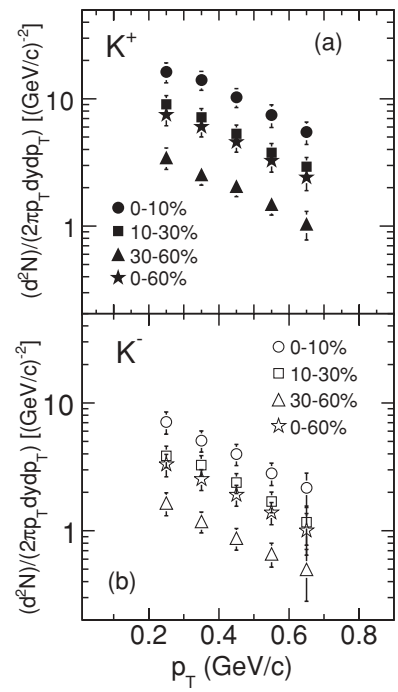

FIG. 9. Transverse momentum spectra for (a) positive kaons and (b) negative kaons at midrapidity ($|y| < 0.5$) in Au + Au collisions at $\sqrt{s_{NN}} = 9.2$ GeV for various centralities. The errors shown are statistical and systematic errors (discussed in Sec. II H) added in quadrature.

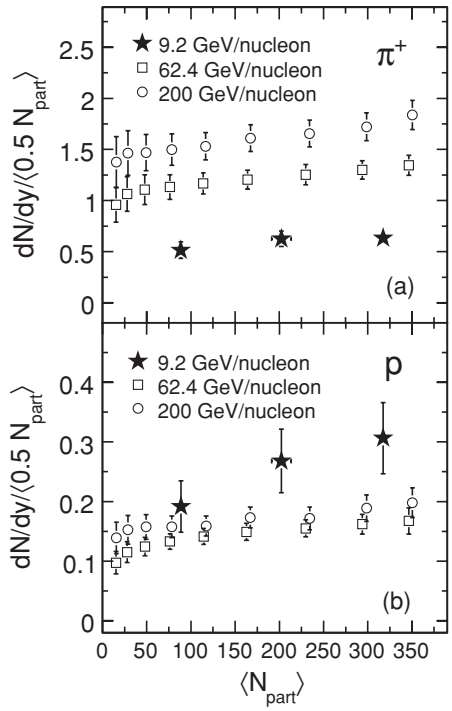

FIG. 10. dN/dy of (a) π^+ and (b) p, normalized by $\langle N_{\rm part}\rangle/2$, for Au + Au collisions at $\sqrt{s_{NN}} = 9.2$ GeV, plotted as a function of $\langle N_{\rm part}\rangle$. The lower energy results are compared with corresponding results for Au + Au collisions at $\sqrt{s_{NN}} = 62.4$ and 200 GeV [23,37]. The errors shown are the quadrature sum of statistical and systematic uncertainties. The systematic errors on pion and proton yields for $\sqrt{s_{NN}} = 9.2$ GeV data are ~12% and ~20%, respectively, for all the collision centralities studied.

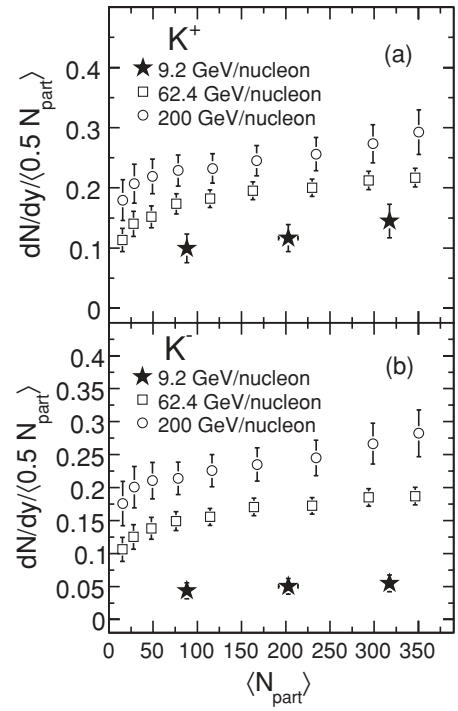

FIG. 11. dN/dy of (a) K^+ and (b) K^-, normalized by $\langle N_{\rm part}\rangle/2$ for Au + Au collisions at $\sqrt{s_{NN}} = 9.2$ GeV, plotted as a function of $\langle N_{\rm part}\rangle$. The lower energy results are compared with corresponding results for Au + Au collisions at $\sqrt{s_{NN}} = 62.4$ and 200 GeV [4,23,37]. The errors shown are the quadrature sum of statistical and systematic uncertainties. The systematic errors on K^+ and K^- yields for $\sqrt{s_{NN}} = 9.2$ GeV data are similar, about 18% for all the collision centralities studied.

by $\langle N_{\rm part}\rangle/2$, between new results at $\sqrt{s_{NN}} = 9.2$ GeV and previously published results at $\sqrt{s_{NN}} = 62.4$ and 200 GeV from the STAR experiment [4,23,37]. The yields of charged pions and kaons decrease with decreasing collision energy. The collision centrality dependence within the limited centrality region studied for the new results is similar to that at higher beam energies. For protons, the yield is larger in central Au + Au collisions at $\sqrt{s_{NN}} = 9.2$ GeV compared to corresponding results at $\sqrt{s_{NN}} = 62.4$ and 200 GeV [4,23,37]. For the most peripheral collisions, the yields are comparable within errors to corresponding yields at higher beam energies. The increase in proton yield with the increasing collision centrality is due to large net-proton ($p - \bar{p}$) density at midrapidity in the lower collision energies.

The inclusive $dN_{\rm ch}/d\eta$ [sum of contributions from $\pi^{\pm}$, $K^{\pm}$, and p ($\bar{p}$) found by redoing the analysis binned in η instead of rapidity] at midrapidity for various collision centralities are given in Table IV along with the statistical and systematic errors for Au + Au collisions at $\sqrt{s_{NN}} = 9.2$ GeV.

Figures 12 and 13 show the comparison of $\langle p_T\rangle$ as a function of $\langle N_{\rm part}\rangle$ for π^+, K^+, and p from Au + Au collisions at $\sqrt{s_{NN}} = 9.2$ GeV with those from collisions at $\sqrt{s_{NN}} = 62.4$ and 200 GeV [4,23,37]. For the collision centralities studied, the dependencies of $\langle p_T\rangle$ on $\langle N_{\rm part}\rangle$ at $\sqrt{s_{NN}} = 9.2$ GeV are similar to those at $\sqrt{s_{NN}} = 62.4$ and 200 GeV. An increase in $\langle p_T\rangle$ with increasing hadron mass is observed at $\sqrt{s_{NN}} =$ 9.2 GeV. A similar dependence is also observed for $\sqrt{s_{NN}} =$ 62.4 and 200 GeV. However, the differences in $\langle p_T\rangle$ between protons and kaons are much smaller than the observations at higher beam energies. The mass dependence of $\langle p_T\rangle$ reflects collective expansion in the radial direction. The smaller difference between $\langle p_T\rangle$ of protons and kaons at $\sqrt{s_{NN}} =$ 9.2 GeV indicates that the average collective velocity in the radial direction is smaller at that energy.

Figures 14 and 15 show the various particle ratios (K^-/K^+, K^-/π^-, p/π^+, and K^+/π^+) as a function of collision centrality expressed as $\langle N_{\rm part}\rangle$ for Au + Au collisions at $\sqrt{s_{NN}} =$ 9.2 GeV. Corresponding results from Au + Au collisions at $\sqrt{s_{NN}} = 62.4$ and 200 GeV [4,23,37] are also shown. The π^-/π^+ ratio is close to unity and is not shown. Due to low event statistics and the low yield of antiprotons, the centrality dependence of the $\bar{p}/p$ ratio for $\sqrt{s_{NN}} = 9.2$ GeV collisions could not be extracted.

TABLE IV. Centrality dependence of $dN_{\rm ch}/d\eta$ at midrapidity in Au + Au collisions at $\sqrt{s_{NN}} = 9.2$ GeV.

% cross section	$dN_{\rm ch}/d\eta$	Stat. error	Sys. error
0–10	229	25	62
10–30	133	15	36
30–60	48	5	13

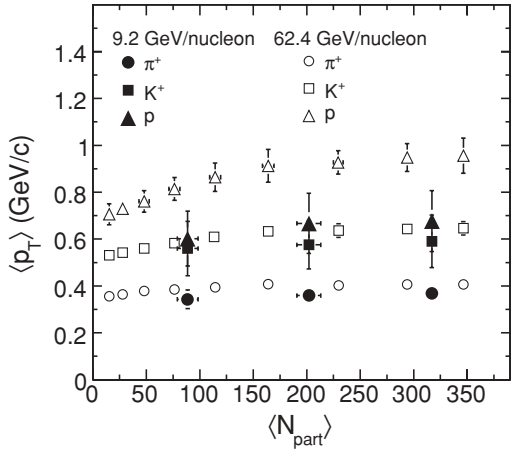

FIG. 12. $\langle p_T \rangle$ for π^+, K^+, and p plotted as a function of $\langle N_{\rm part} \rangle$ for Au + Au collisions at $\sqrt{s_{NN}} = 9.2$ GeV and compared with corresponding results at $\sqrt{s_{NN}} = 62.4$ GeV [4,23,37]. The errors shown are the quadrature sum of statistical and systematic uncertainties. The systematic errors for pions, kaons, and protons for $\sqrt{s_{NN}} = 9.2$ GeV are ∼12%, 18%, and 21%, respectively, and similar for all the collision centralities studied.

The K^-/K^+ and K^-/π^- ratios are lower at $\sqrt{s_{NN}} = 9.2$ GeV than those at $\sqrt{s_{NN}} = 62.4$ and 200 GeV. In the case of K^+/π^+, there is less variation between 9.2 GeV and the highest RHIC energies than in case of the other particle ratios discussed above. This reflects an interplay between the decreasing importance of associated production and an increasing contribution from pair production of kaons with increasing collision energy. Associated production refers to reactions such as $NN \rightarrow KYN$ and $\pi N \rightarrow KY$, where N is a nucleon and Y a hyperon. The p/π^+ ratio is larger at $\sqrt{s_{NN}} = 9.2$ GeV than at $\sqrt{s_{NN}} = 62.4$ and 200 GeV for all collision centralities studied. As discussed above, this is a consequence of higher net-proton density at midrapidity for the collisions at $\sqrt{s_{NN}} = 9.2$ GeV than for those at $\sqrt{s_{NN}} = 62.4$ and 200 GeV.

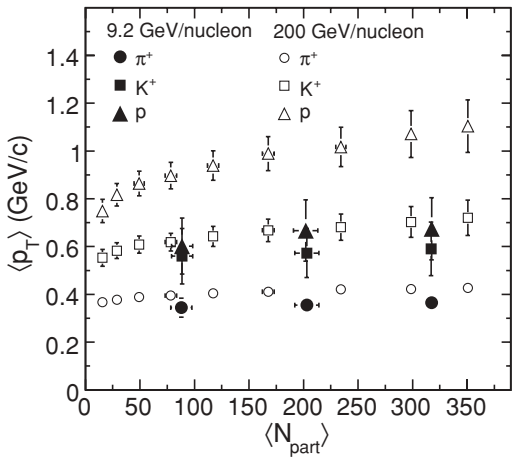

FIG. 13. $\langle p_T \rangle$ for π^+, K^+ and p plotted as a function of $\langle N_{\rm part} \rangle$ for Au + Au collisions at $\sqrt{s_{NN}} = 9.2$ GeV and compared with corresponding results at $\sqrt{s_{NN}} = 200$ GeV [4,23,37]. The errors shown are the quadrature sum of statistical and systematic uncertainties. The systematic errors for pions, kaons, and protons for $\sqrt{s_{NN}} = 9.2$ GeV are ∼12%, 18%, and 21%, respectively, and similar for all the collision centralities studied.

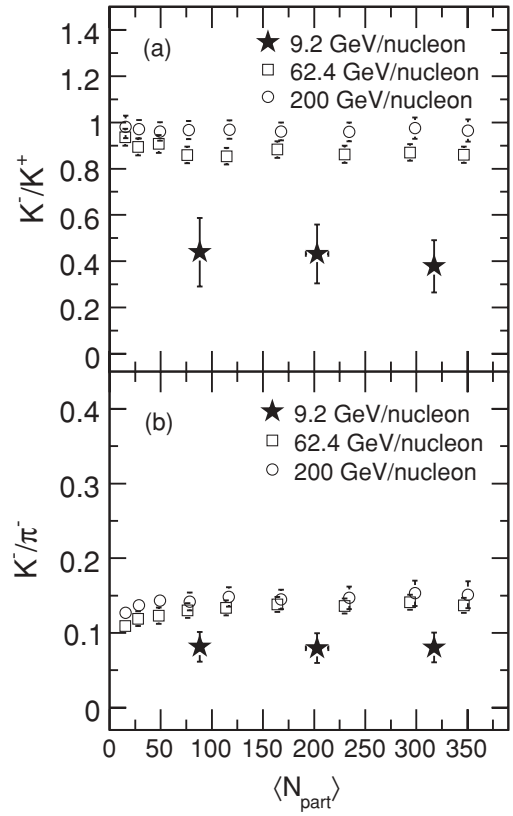

FIG. 14. Variation of (a) K^-/K^+ and (b) K^-/π^- ratios as a function of $\langle N_{\rm part} \rangle$ for Au + Au collisions at $\sqrt{s_{NN}} = 9.2$ GeV. For comparison we also show the corresponding results from Au + Au collisions at $\sqrt{s_{NN}} = 62.4$ and 200 GeV [23,37]. The errors shown are the quadrature sum of statistical and systematic uncertainties. The systematic errors for K^-/K^+ and K^-/π^- for $\sqrt{s_{NN}} = 9.2$ GeV data are ∼25% and 22%, respectively, and similar for all the collision centralities studied.

C. Energy dependence of particle production

Figure 16 shows the $dN_{\rm ch}/d\eta$ at midrapidity normalized by $\langle N_{\rm part} \rangle/2$ as a function of $\sqrt{s_{NN}}$. The result from $\sqrt{s_{NN}} = 9.2$ GeV is in agreement with the general energy dependence trend observed at the BNL Alternating Gradient Synchrotron (AGS) [38], CERN Super Proton Synchrotron (SPS) [39], and RHIC [23,40]. The result at 9.2 GeV has a value close to that obtained at a similar energy ($\sqrt{s_{NN}} = 8.8$ GeV) by the NA49 experiment at SPS [39]. Figures 17(a) and 18(a) show dN/dy normalized by $\langle N_{\rm part} \rangle/2$ for $\pi^\pm$ and $K^\pm$, respectively, in 0–10% central Au + Au collisions at $\sqrt{s_{NN}} = 9.2$ GeV, compared with previous results at AGS [38], SPS [39], and RHIC [23]. Within errors, the yields are consistent with previous results at similar $\sqrt{s_{NN}}$. Figures 17(b) and 18(b) show the $\langle m_T \rangle - m$ for $\pi^\pm$ and $K^\pm$, respectively, in 0–10% central Au + Au collisions at $\sqrt{s_{NN}} = 9.2$ GeV. The results are also compared with previous measurements at various energies.

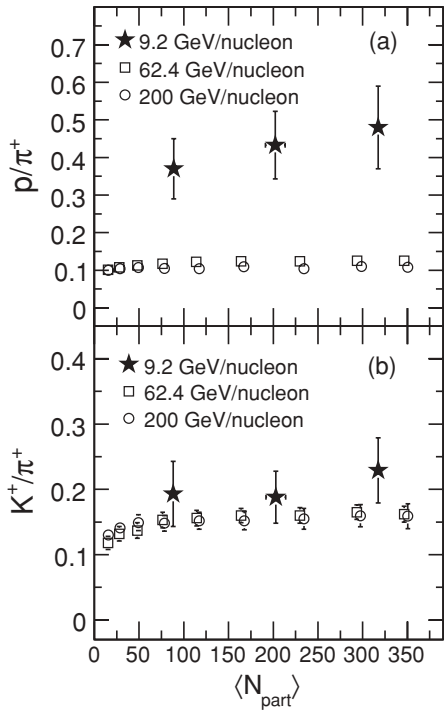

FIG. 15. Variation of (a) p/π^+ and (b) K^+/π^+ ratios as a function of $\langle N_{\rm part}\rangle$ for Au + Au collisions at $\sqrt{s_{NN}} = 9.2$ GeV. For comparison, we also show the corresponding results from Au + Au collisions at $\sqrt{s_{NN}} = 62.4$ and 200 GeV [4,23,37]. The errors shown are the quadrature sum of statistical and systematic uncertainties. The systematic errors for p/π^+ and K^+/π^+ for $\sqrt{s_{NN}} = 9.2$ GeV data are ∼25% and 22%, respectively, and similar for all the collision centralities studied.

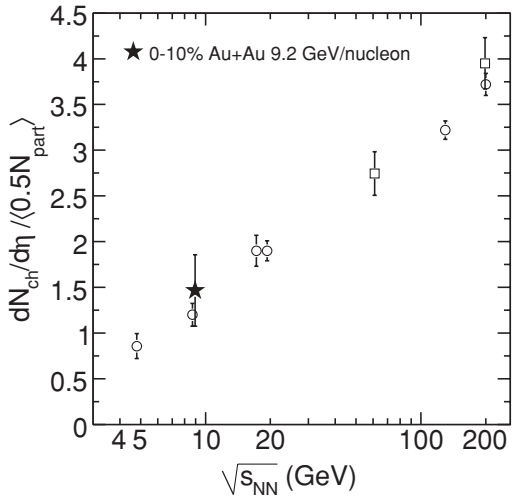

FIG. 16. Midrapidity $dN_{\rm ch}/d\eta$ normalized by $\langle N_{\rm part}\rangle/2$ as a function of $\sqrt{s_{NN}}$. Au + Au collisions at $\sqrt{s_{NN}} = 9.2$ GeV are compared with previous results from AGS [38], SPS [39], and RHIC [23,40]. The errors shown are the quadrature sum of statistical and systematic uncertainties. The systematic error for $\sqrt{s_{NN}} = 9.2$ GeV data is 39%.

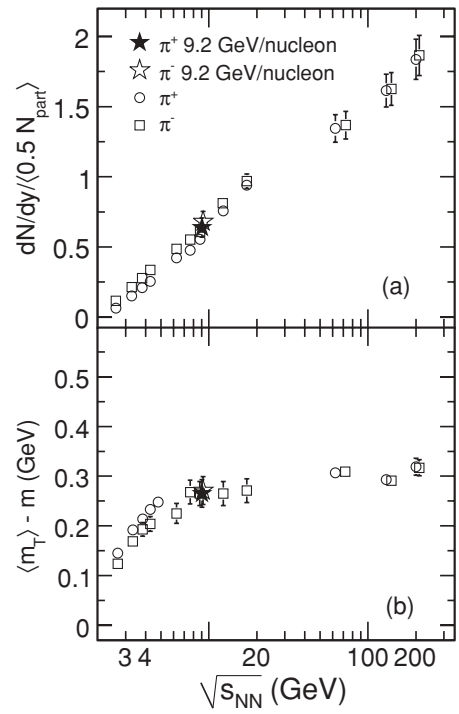

FIG. 17. (a) dN/dy normalized by $\langle N_{\rm part}\rangle/2$ and (b) $\langle m_T\rangle - m$ of $\pi^\pm$, in 0–10% central Au + Au collisions for $\sqrt{s_{NN}} = 9.2$ GeV compared with previous results from AGS [38], SPS [39], and RHIC [23]. The errors shown are the quadrature sum of statistical and systematic uncertainties.

The results from Au + Au collisions at $\sqrt{s_{NN}} = 9.2$ GeV are consistent with corresponding measurements at SPS energies at similar $\sqrt{s_{NN}}$. Both dN/dy and $\langle m_T\rangle - m$ are obtained using data in the measured p_T ranges and extrapolations assuming certain functional forms for the unmeasured p_T ranges, as discussed in Sec. V B of our previous paper [23]. For the present midrapidity measurements, the percentage contribution to the yields from extrapolation are about 20% for $\pi^\pm$, 50% for $K^\pm$, and 25% for p.

The $\langle m_T\rangle - m$ values increase with $\sqrt{s_{NN}}$ at lower AGS energies, stay independent of $\sqrt{s_{NN}}$ at the SPS and RHIC 9.2 GeV collisions, then tend to rise further with increasing $\sqrt{s_{NN}}$ at the higher beam energies at RHIC. For a thermodynamic system, $\langle m_T\rangle - m$ can be an approximate representation of the temperature of the system, and $dN/dy \propto \ln(\sqrt{s_{NN}})$ may represent its entropy. In such a scenario, the observations could reflect the characteristic signature of a first-order phase transition, as proposed by Van Hove [41]. Then the constant value of $\langle m_T\rangle - m$ vs $\sqrt{s_{NN}}$ around 9.2 GeV has one possible interpretation in terms of formation of a mixed phase of a QGP and hadrons during the evolution of the heavy-ion system. However, there could be several other effects to which $\langle m_T\rangle - m$ is sensitive, which also need to be understood for proper interpretation of the data [42]. The energy dependencies of the proton dN/dy and $\langle m_T\rangle - m$ are not discussed in this paper, as the STAR results are presented without correction for feed-down contributions. The low event statistics in the present data does not allow us to obtain feed-down corrections from the data itself. All results presented in this paper are from

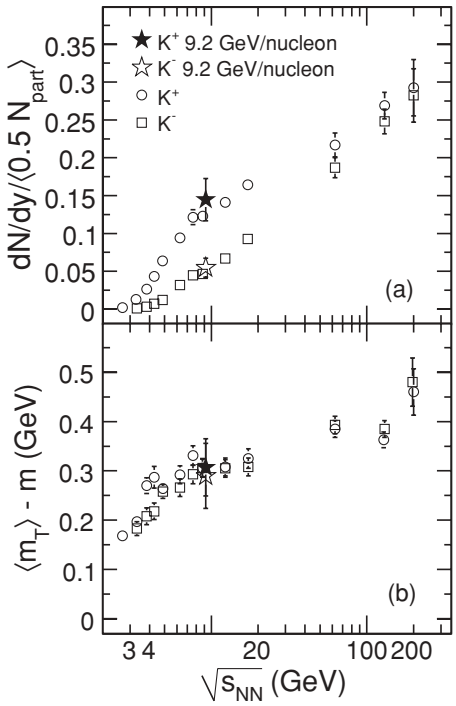

FIG. 18. (a) dN/dy normalized by $\langle N_{\rm part}\rangle/2$ and (b) $\langle m_T\rangle - m$ of $K^{\pm}$, in 0–10% central Au + Au collisions for $\sqrt{s_{NN}} = 9.2$ GeV compared with previous results from AGS [38], SPS [39], and RHIC [23]. The errors shown are the quadrature sum of statistical and systematic uncertainties.

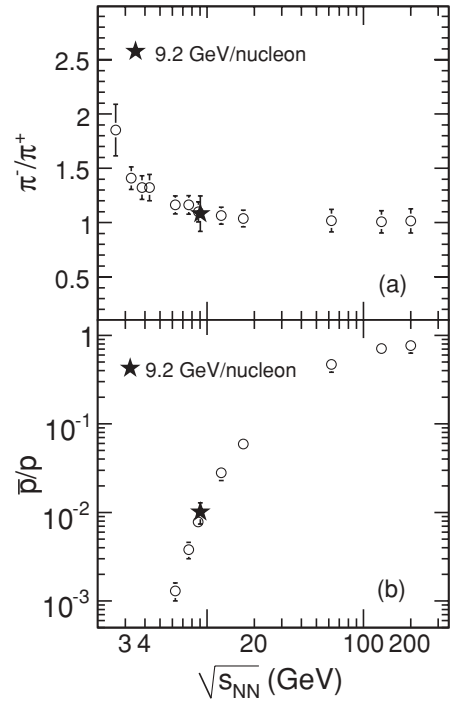

FIG. 19. (a) π^-/π^+ and (b) $\bar{p}/p$ ratios at midrapidity ($|y| < 0.5$) for central 0–10% Au + Au collisions at $\sqrt{s_{NN}} = 9.2$ GeV compared with previous results from AGS [38], SPS [39], and RHIC [23]. The errors shown are the quadrature sum of statistical and systematic uncertainties. The systematic errors on π^-/π^+ and $\bar{p}/p$ for $\sqrt{s_{NN}} =$ 9.2 GeV data are 15% and 27%, respectively.

inclusive protons and antiprotons as in our previous paper at higher energies at RHIC [23].

Figures 19(a) and 19(b) show the collision energy dependence of the particle ratios π^-/π^+ and $\bar{p}/p$, respectively, in central heavy-ion collisions. Similarly, Figs. 20(a) and 20(b) show the ratios of K^-/K^+ and K/π, respectively. The new results from Au + Au collisions at $\sqrt{s_{NN}} = 9.2$ GeV follow the $\sqrt{s_{NN}}$ trend established by previous measurements. The p_T-integrated π^-/π^+ ratio at $\sqrt{s_{NN}} = 9.2$ GeV is 1.08 ± 0.04 (stat.) $\pm$ 0.16 (sys.). Those at lower beam energies have values much larger than unity, which could be due to significant contributions from resonance decays (such as from Δ baryons). The value of the $\bar{p}/p$ ratio at $\sqrt{s_{NN}} =$ 9.2 GeV is 0.010 ± 0.001 (stat.) $\pm$ 0.003 (sys.) indicating large values of net-protons. The $\bar{p}/p$ ratio increases with increasing collision energy and approaches unity for top RHIC energies. This indicates that at higher beam energies, the p ($\bar{p}$) production at midrapidity is dominated by pair production. The K^-/K^+ ratio at $\sqrt{s_{NN}} = 9.2$ GeV is 0.38 ± 0.05 (stat.) $\pm$ 0.09 (sys.), indicating a significant contribution to kaon production from associated production at lower collision energies. With increasing $\sqrt{s_{NN}}$, the K^-/K^+ ratio approaches unity, indicating dominance of kaon pair production. The K/π ratio is of interest, as it expresses the enhancement of strangeness production relative to nonstrange hadrons in heavy-ion collisions compared to $p + p$ collisions. The increase in the K^+/π^+ ratio with beam energies up to $\sqrt{s_{NN}} = 7.7$ GeV at SPS, and the subsequent decrease and possible saturation with increasing beam energies has been the subject of intense theoretical debate recently [39,43]. The discussions mainly focus on the question of the relevant degrees of freedom that are necessary to explain the energy dependence of the K/π ratio. Our new results from Au + Au collisions at $\sqrt{s_{NN}} = 9.2$ GeV with only about 3000 events (hence with large errors) are found to be consistent with the previously observed energy dependence.

D. Azimuthal anisotropy

The study of collective flow in relativistic nuclear collisions could provide insights into the equation of state (EOS) of the matter created by the collisions. As discussed earlier, there are two types of azimuthal anisotropy that are widely studied in heavy-ion collisions, directed flow v_1 and elliptic flow v_2. Directed flow measurements at forward rapidities describe the "side-splash" motion of the collision products. Hence, it is an important tool for probing the dynamics of the system at forward rapidities [44]. Since v_1 is generated very early in the evolution of heavy-ion collisions, it probes the onset of bulk collective dynamics. The shape of v_1 vs rapidity around midrapidity is suggested as a signature of a first-order phase transition [45]. On the other hand, the characterization of the elliptic flow of produced particles by their azimuthal anisotropy has proven to be one of the most successful probes of the dynamics in Au + Au collisions at RHIC [25,46–52]. Elliptic flow provides the possibility of gaining information about the degree of thermalization of the hot, dense medium.

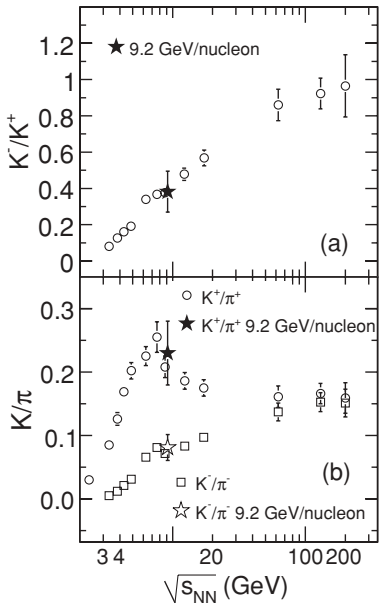

FIG. 20. (a) K^-/K^+ and (b) K/π ratios at midrapidity ($|y|<0.5$) for central 0–10% Au + Au collisions at $\sqrt{s_{NN}} = 9.2$ GeV compared with previous results from AGS [38], SPS [39], and RHIC [23]. The errors shown are the quadrature sum of statistical and systematic uncertainties. The systematic errors on K^-/K^+ and K/π for $\sqrt{s_{NN}} = 9.2$ GeV data are 23% and 19%, respectively.

Studying its dependence on system size, number of constituent quarks, transverse momentum, and transverse mass, is crucial to the understanding of the properties of the produced matter.

Figure 21 shows charged-hadron v_1 results in Au + Au collisions for the 0–60% collision centrality at $\sqrt{s_{NN}} =$ 9.2 GeV, compared with corresponding results from 30–60% central Au + Au collisions at $\sqrt{s_{NN}} = 62.4$ and 200 GeV [53].

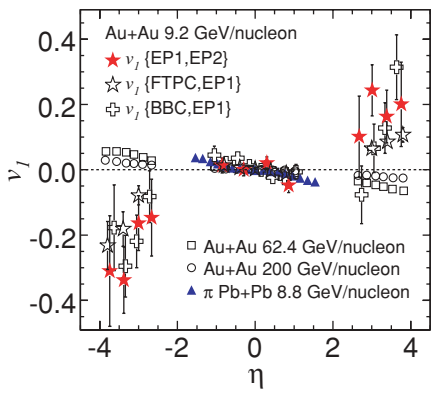

FIG. 21. (Color online) Charged-hadron v_1 vs η from the 0–60% collision centrality Au + Au collisions at $\sqrt{s_{NN}} = 9.2$ GeV. The errors shown are statistical. Systematic errors are discussed in Sec. II H. The solid star symbols are the results obtained from the mixed harmonic method, while the open star and open plus symbols represent results from the standard methods (see text for details). The results are compared to v_1 from 30–60% collision centrality Au + Au collisions at $\sqrt{s_{NN}} = 62.4$ and 200 GeV [53]. For comparison, v_1 for charged pions for the 0–60% collision centrality from Pb + Pb collisions at $\sqrt{s_{NN}} = 8.8$ GeV are also shown [54].

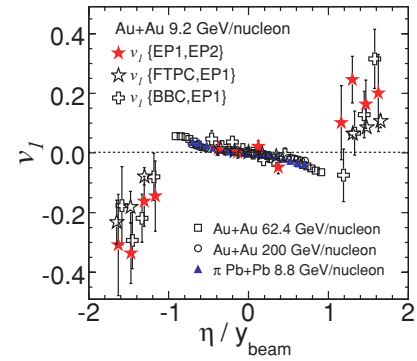

FIG. 22. (Color online) Same as Fig. 21, but plotted as a function of η/y_{beam}.

The p_T range of this study is 0.15–2.0 GeV/c. The v_1 results from Au + Au collisions at $\sqrt{s_{NN}} = 9.2$ GeV are shown for the three different methods, as described in Sec. II E. The results from the three methods are consistent within the error bars. These results are also compared with v_1 for charged pions in Pb + Pb collisions at $\sqrt{s_{NN}} = 8.8$ GeV measured by NA49 [54]. At midrapidity, all the results have comparable values. At forward rapidity ($|\eta| > 2$), the trend of v_1 for higher $\sqrt{s_{NN}}$ (62.4 and 200 GeV) appears to be different from that for $\sqrt{s_{NN}} = 9.2$ GeV. This can be explained by contributions from spectator protons to the directed flow signal at large $|\eta|$. The beam rapidities y_{beam} for $\sqrt{s_{NN}} = 9.2$, 62.4, and 200 GeV are 2.3, 4.2, and 5.4, respectively. With η divided by the respective y_{beam} values for the beam energies (Fig. 22), all the v_1 values follow a common trend for the measured $|\eta|/y_{\text{beam}} < 1$ range.

Figure 23 shows $v_2(p_T)$ for charged hadrons, pions, and protons in $\sqrt{s_{NN}} = 9.2$ GeV collisions. For comparison, we show pion v_2 results from NA49 [54] at similar $\sqrt{s_{NN}}$. Within the statistical errors, there is good agreement between results from the two experiments. At top RHIC energies, v_2 at low p_T shows a characteristic scaling with particle mass [5] that is consistent with hydrodynamic behavior; however, the available statistics in the current analysis are insufficient to extend this study to 9.2 GeV. The small number of events also precludes the extension of the measurements to larger p_T values, to study the number of constituent quark scaling of v_2 observed at $\sqrt{s_{NN}} = 200$ GeV. Figure 24 shows the elliptic flow parameter at $\sqrt{s_{NN}} = 9.2$ GeV compared with other beam energies [46,50,54,56–58]. The STAR data at $\sqrt{s_{NN}} = 9.2$ GeV, denoted by the star symbol, follow the observed $\sqrt{s_{NN}}$ dependence.

E. Pion interferometry

Information about the space-time structure of the emitting source can be extracted with intensity interferometry techniques [59]. The primary goal of pion interferometry, performed at midrapidity and at low transverse momentum, is to study the space-time size of the emitting source and freeze-out processes of the dynamically evolving collision fireball. The three-dimensional correlation functions are fitted with Eq. (13), where R_i is the homogeneity length in the i direction [28–30]. Projections of the fit to the correlation function of

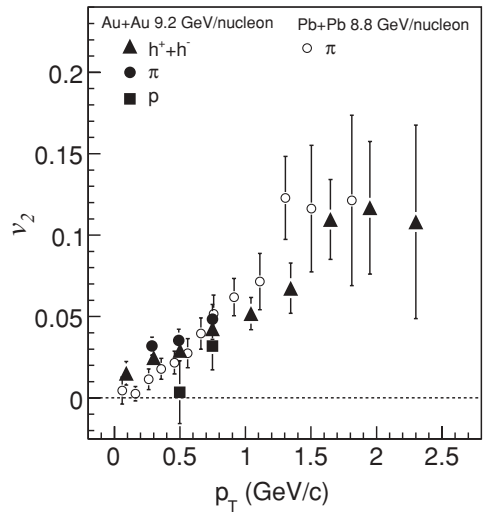

FIG. 23. v_2 as a function of p_T for charged hadrons (solid triangles), π (solid circles), and p (solid squares) in 0–60% Au + Au collisions at $\sqrt{s_{NN}} = 9.2$ GeV. The error bars include only statistical uncertainties for $\sqrt{s_{NN}} = 9.2$ GeV data. The corresponding systematic error is discussed in Sec. II H. For comparison, $v_2(p_T)$ results for π (open circles) from NA49 [54] in 0–43.5% Pb + Pb collisions at $\sqrt{s_{NN}} = 8.8$ GeV are also shown.

the 0–60% most central collisions, weighted according to the mixed-pair background, are shown in Fig. 25. The three panels show the projections of the three-dimensional correlation function onto the $q_{\rm out}$, $q_{\rm side}$, and $q_{\rm long}$ axes. The curves show Bowler-Sinyukov fits [34] to the Coulomb-corrected correlation function. Table V lists the Hanbury-Brown–Twiss (HBT) parameters obtained from the fits along with statistical errors.

The radius parameter $R_{\rm side}$ has the most direct correlation with the source geometry, whereas $R_{\rm out}$ encodes both geometry and time scale. Hydrodynamic calculations with a first-order

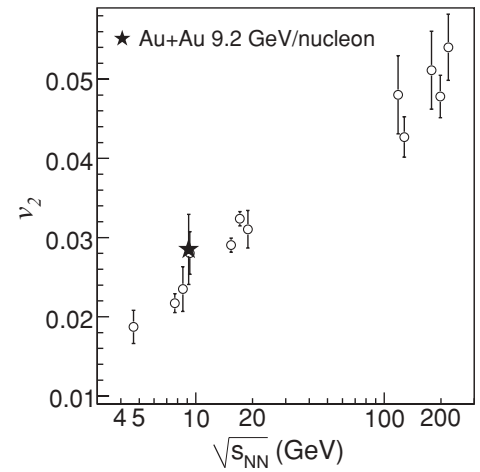

FIG. 24. Energy dependence of v_2 near midrapidity ($-1 < \eta < 1$) for $\sqrt{s_{NN}} = 9.2$ GeV 0–60% central Au + Au collisions. Only statistical errors are shown. The results of STAR charged-hadron v_2 [55] are compared with those measured by E877 [56], NA49 [54], PHENIX [57], and PHOBOS [46,50,58] collaborations.

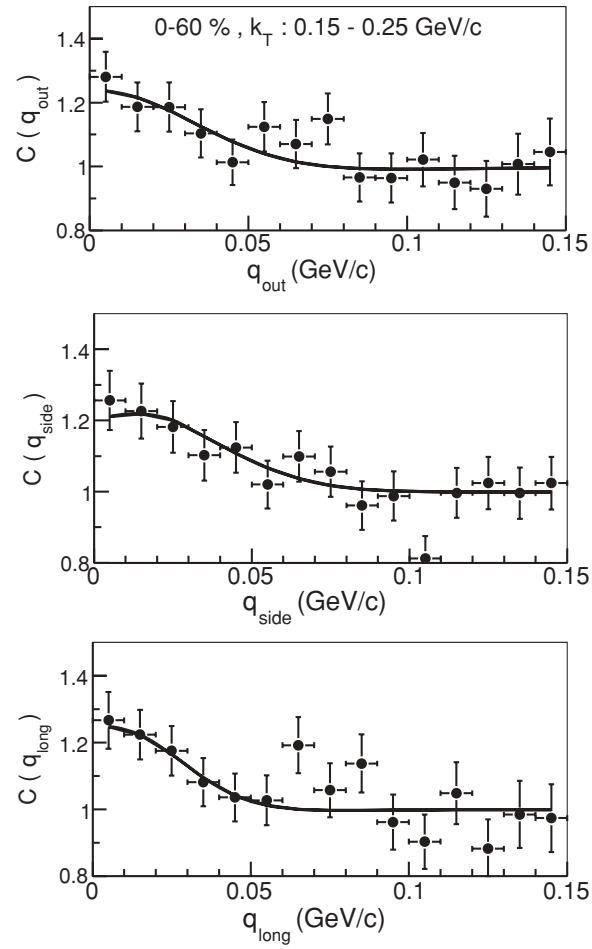

FIG. 25. Projections of the three-dimensional correlation function and corresponding Bowler-Sinyukov [34] fits (lines) for negative pions from the 0–60% central Au + Au events and $k_T = [150, 250]$ MeV/c.

phase transition predict a ratio of $R_{\rm out}/R_{\rm side}$ larger than unity. Our measurements indicate the ratio $R_{\rm out}/R_{\rm side} = 1.4 \pm 0.4$.

IV. FREEZE-OUT PARAMETERS AND PHASE DIAGRAM

The measured hadron spectra reflect the properties of the bulk matter at kinetic freeze-out, after elastic collisions among the hadrons have ceased. More direct information on the earlier stages can be deduced from the integrated yields of the different hadron species, which change only via inelastic collisions. The point in time at which these inelastic collisions cease is referred to as chemical freeze-out, which takes place before kinetic freeze-out. The transverse momentum distributions of the different particles contain two components,

TABLE V. HBT parameters for 0–60% central events and $150 < k_T < 250$ MeV/c.

λ	$R_{\rm out}$ (fm)	$R_{\rm side}$ (fm)	$R_{\rm long}$ (fm)
0.36 ± 0.08	5.05 ± 0.96	3.52 ± 0.56	3.25 ± 0.86

one random and one collective. The random component can be identified as the one that depends on the temperature of the system at kinetic freeze-out ($T_{\rm kin}$). The collective component, which arises from the matter density gradient from the center to the boundary of the fireball created in high-energy nuclear collisions, is generated by collective flow in the transverse direction and is characterized by its velocity β_T.

Assuming that the system attains thermal equilibrium, the blast-wave (BW) formulation [60] can be used to extract $T_{\rm kin}$ and $\langle\beta_T\rangle$. The transverse flow velocity of a particle at a distance r from the center of the emission source, as a function of the surface velocity β_s of the expanding cylinder, is parametrized as $\beta_T(r) = \beta_s(r/R)^n$, where n is found by fitting the data. The transverse momentum spectrum is then

$$\frac{dN}{p_T dp_T} \propto \int_0^R r\, dr\, m_T I_0\left(\frac{p_T \sinh\rho(r)}{T_{\rm kin}}\right) \times K_1\left(\frac{m_T \cosh\rho(r)}{T_{\rm kin}}\right), \qquad (14)$$

where I_0 and K_1 are modified Bessel functions and $\rho(r) = \tanh^{-1}\beta_T(r)$. Simultaneous fits to the p_T distributions of π, K, and p at midrapidity for central 0–10% Au + Au collisions at $\sqrt{s_{NN}} = 9.2$ GeV are shown in Fig. 26. The extracted parameters are $T_{\rm kin} = 105 \pm 10$ (stat.) $\pm$ 16 (sys.) MeV, $\langle\beta_T\rangle = 0.46c \pm 0.01c$ (stat.) $\pm$ $0.04c$ (sys.), and $n = 0.9 \pm 6.4$ (stat.) $\pm$ 6.4 (sys.) with $\chi^2/{\rm ndf} = 15/17$. The parameter n is poorly constrained by the fits in this low-event statistical data set. The parameter values do not change within the quoted errors for other centrality ranges. Only statistical errors are used for obtaining the fit parameters shown in the figure. Inclusion of systematic errors gives similar values of $T_{\rm kin}$ and $\langle\beta_T\rangle$. Similar studies have been done for other higher energy collisions at RHIC [23].

Within a statistical model in thermodynamic equilibrium, the particle abundance in a system of volume V can be given

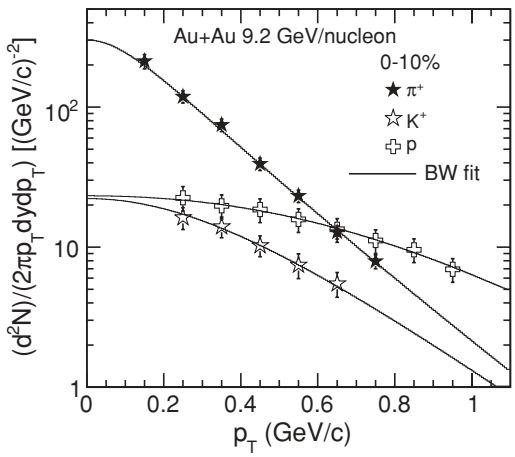

FIG. 26. Midrapidity transverse momentum distributions of pions, kaons, and protons (no feed-down correction) for 0–10% most central Au + Au collisions at $\sqrt{s_{NN}} = 9.2$ GeV, fitted to blast-wave model calculations [60]. The extracted kinetic freeze-out parameters are $T_{\rm kin} = 105 \pm 10$ (stat.) $\pm$ 16 (sys.) MeV and $\langle\beta_T\rangle = 0.46c \pm 0.01c$ (stat.) $\pm$ $0.04c$ (sys.).

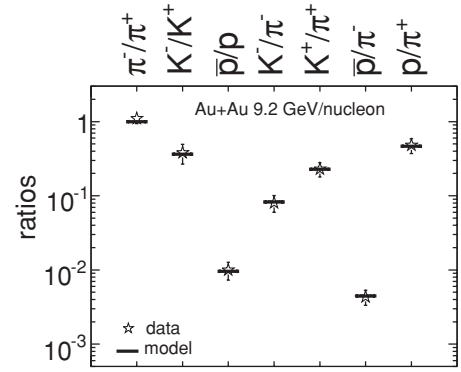

FIG. 27. Midrapidity particle ratios for 0–10% most central Au + Au collisions at $\sqrt{s_{NN}} = 9.2$ GeV, fitted to thermal model calculations. See text for details. The extracted chemical freeze-out temperature is $T_{\rm ch} = 151 \pm 2$ (stat.) $\pm$ 7 (sys.) MeV and baryon chemical potential is $\mu_B = 354 \pm 7$ (stat.) $\pm$ 30 (sys.) MeV.

by

$$\frac{N_i}{V} = \frac{g_i}{(2\pi)^3}\gamma_S^{S_i}\int \frac{1}{\exp\left(\frac{E_i - \mu_B B_i - \mu_S S_i}{T_{\rm ch}}\right) \pm 1} d^3p, \qquad (15)$$

where N_i is the abundance of particle species i, g_i is the spin degeneracy, B_i and S_i are the baryon number and strangeness number, respectively, E_i is the particle energy, and the integral is taken over all momentum space [23]. The model parameters are the chemical freeze-out temperature $T_{\rm ch}$, the baryon (μ_B) and strangeness (μ_S) chemical potentials, and the *ad hoc* strangeness suppression factor γ_S. Measured particle ratios are used to constrain the values of $T_{\rm ch}$ and μ_B at chemical freeze-out using the statistical model assumption that the system is in thermal and chemical equilibrium at that stage. Fits are performed to the various ratios for midrapidity central 0–10% Au + Au collisions at $\sqrt{s_{NN}} = 9.2$ GeV using such a model and shown in Fig. 27. The analysis is done within the framework of a statistical model as discussed in Ref. [61]. This model has been used to extract chemical freeze-out parameters at higher RHIC energies [23]. The extracted parameter values are $T_{\rm ch} = 151 \pm 2$ (stat.) $\pm$ 7 (sys.) MeV, $\mu_B = 354 \pm 7$ (stat.) $\pm$ 30 (sys.) MeV, $\mu_S = 25 \pm 9$ (stat.) $\pm$ 14 (sys.) MeV, and $\gamma_S = 0.9 \pm 0.7$ (stat.) $\pm$ 0.1 (sys.) for 9.2 GeV data. These values are very close to those extracted from the measurements at SPS for similar $\sqrt{s_{NN}}$ [62]. Only statistical errors on the particle production ratios are used for obtaining the fit parameters. Inclusion of systematic errors gives similar values of $T_{\rm ch}$ and μ_B.

Figure 28 shows the temperatures at various stages in heavy-ion collisions as a function of μ_B (at different $\sqrt{s_{NN}}$). The μ_B values shown were estimated at chemical freeze-out. The initial temperatures $T_{\rm initial}$ achieved at top RHIC and SPS energies are obtained from models [63] that explain the direct photon measurements from the PHENIX experiment at RHIC [64] and from the WA98 experiment at SPS [65]. From these models, which assume that thermalization is achieved in the collisions within a time between 0.1 and 1.2 fm/c, the $T_{\rm initial}$ extracted is greater than 300 MeV at RHIC and greater than 200 MeV at SPS. The $T_{\rm ch}$ and $T_{\rm kin}$ values extracted from

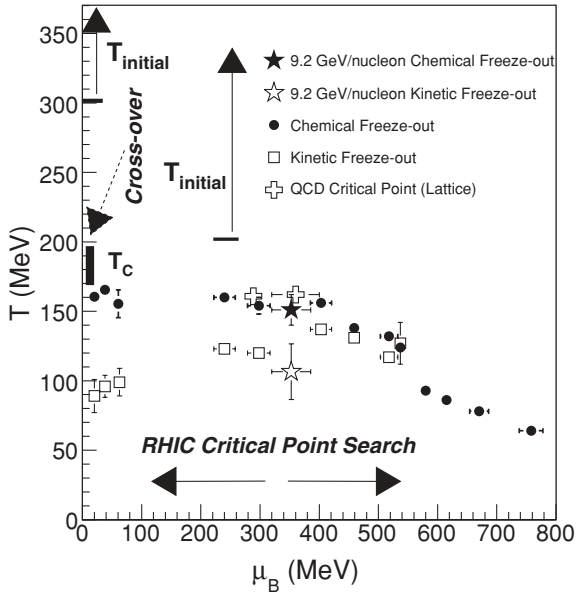

FIG. 28. Temperature vs baryon chemical potential (μ_B) from heavy-ion collisions at various $\sqrt{s_{NN}}$ [23]. The μ_B values were estimated at chemical freeze-out. The kinetic and chemical freeze-out parameters, extracted using models assuming thermal and chemical equilibrium from midrapidity measurement in central 0–10% Au + Au collisions at $\sqrt{s_{NN}} = 9.2$ GeV, are shown as star symbols. The range of critical temperatures (T_c) [66] of the crossover quark-hadron phase transition at $\mu_B = 0$ [6] and the QCD critical point from two different calculations [9] from lattice QCD are also indicated. Model-based estimates of the range of initial temperature (T_{initial}) achieved in heavy-ion collisions based in part on direct photon data at top RHIC [64] and SPS [65] energies are also shown. The range of μ_B to be scanned in the upcoming RHIC critical-point search and beam energy scan program corresponding to $\sqrt{s_{NN}} = 5.5$–39 GeV is indicated by horizontal arrows near the μ_B axis [12].

particle ratios and p_T spectra of various hadrons, respectively, from models assuming thermodynamical equilibrium are also shown. The values for $\sqrt{s_{NN}} = 9.2$ GeV are from the data presented in this paper. The values at other $\sqrt{s_{NN}}$ are from Ref. [23] and references therein. It is interesting to observe that T_{ch} and T_{kin} values approach each other in the high μ_B regime. A few recent predictions from lattice QCD calculations [10] are also shown in Fig. 28. Several lattice QCD calculations indicate that the partonic-to-hadronic phase transition occurs around $T_c \sim 170$–190 MeV [66]. These calculations also suggest that the phase transition at $\mu_B = 0$ is a crossover [6]. Most QCD-based model calculations [3,7] suggest that the phase transition at large μ_B is of first order. Two estimates of the QCD critical point [9] in the T-μ_B plane taking $T_c = 176$ MeV are shown in Fig. 28. The region planned to be explored in the critical-point search program at RHIC is shown in Fig. 28.

V. SUMMARY AND OUTLOOK

We have presented measurements of identified particle production, azimuthal anisotropy, and pion interferometry in Au + Au collisions at $\sqrt{s_{NN}} = 9.2$ GeV. The results are obtained from only about 3000 events from the lowest beam energy run to date at the RHIC facility. The transverse momentum spectra of pions, kaons, and protons are presented for 0–10%, 10–30%, 30–60%, and 0–60% collision centrality classes. The bulk properties are studied by measuring the identified hadron dN/dy, $\langle p_T \rangle$, particle ratios, v_1 (also at forward rapidity), v_2, and HBT radii (R_{out}, R_{side}, and R_{long}). All measurements are consistent with the corresponding previous results from fixed-target experiments at similar $\sqrt{s_{NN}}$.

The $\langle p_T \rangle$ for protons is higher than that for pions, indicating some degree of collective flow in the radial direction. However, the difference between $\langle p_T \rangle$ for protons and kaons is considerably smaller at $\sqrt{s_{NN}} = 9.2$ GeV than at $\sqrt{s_{NN}} = 62.4$ and 200 GeV at RHIC. This suggests that the average collective velocity in the radial direction at the lower beam energy is smaller than that for 62.4 and 200 GeV collisions.

The $\bar{p}/p$ ratio at midrapidity for $\sqrt{s_{NN}} = 9.2$ GeV collisions is much smaller, with a value of 0.010 ± 0.001 (stat.) $\pm$ 0.003 (sys.), and the p/π^+ ratio is larger than for Au + Au collisions at $\sqrt{s_{NN}} = 200$ GeV. These measurements indicate large net-proton density at midrapidity in collisions at $\sqrt{s_{NN}} =$ 9.2 GeV. In this region of high net-baryon density for 9.2 GeV collisions, the dominant channel for kaon production is the associated production. The K^-/K^+ ratio has a value of 0.38 $\pm$ 0.05 (stat.) $\pm$ 0.09 (sys.), and the K^+/π^+ ratio is slightly higher than that in collisions at $\sqrt{s_{NN}} = 200$ GeV.

The directed flow measurements, plotted as a function of pseudorapidity scaled by the beam rapidity, have similar values for three collision energies ($\sqrt{s_{NN}} = 9.2$, 62.4, and 200 GeV). A large v_1 signal is observed at forward rapidities at $\sqrt{s_{NN}} = 9.2$ GeV. These collisions could have significant contribution from protons that dominate at large $|\eta|$ (spectator effects). The v_2 measurements for charged hadrons, pions, and protons are also presented for $\sqrt{s_{NN}} = 9.2$ GeV Au + Au collisions at RHIC. The charged-pion v_2 as a function of p_T is observed to be comparable to that from NA49 at similar collision energy. The STAR data at $\sqrt{s_{NN}} = 9.2$ GeV are also found to follow the existing beam energy dependence of v_2 for charged hadrons.

The pion interferometry results give information of the size of the homogeneity region of the source. The pion HBT radii R_{out}, R_{side}, and R_{long} have values 5.05 ± 0.96, 3.52 ± 0.56, and 3.25 ± 0.86 fm, respectively.

The kinetic freeze-out parameters are extracted from a blast-wave model fit to pion, kaon, and proton p_T spectra. We obtain $T_{\text{kin}} = 105 \pm 10$ (stat.) $\pm$ 16 (sys.) MeV and $\langle \beta_T \rangle = 0.46c \pm 0.01c$ (stat.) $\pm$ $0.04c$ (sys.). The chemical freeze-out parameters are extracted from a thermal model fit to the particle ratios at midrapidity. We extract $T_{\text{ch}} = 151 \pm 2$ (stat.) $\pm$ 7 (sys.) MeV and $\mu_B = 354 \pm 7$ (stat.) $\pm$ 30 (sys.) MeV for 0–10% central Au + Au collisions at $\sqrt{s_{NN}} = 9.2$ GeV.

These results from the lowest energy collisions studied up to now at RHIC demonstrate the capabilities of the STAR detector to pursue the proposed beam energy scan. Large and uniform acceptance for all beam energies in a collider setup, excellent particle identification (augmented by the inclusion of a full-barrel time of flight [67] in addition to the large acceptance TPC), and higher statistics will offer significant quantitative and qualitative improvement over existing data.

The QCD critical-point program at RHIC will allow us to extensively explore the QCD phase diagram. It will also allow us to search for the onset of various observations related to partonic matter that have already been uncovered at the highest RHIC energies.

ACKNOWLEDGMENTS

We thank the RHIC Operations Group and RCF at BNL, and the NERSC Center at LBNL and the resources provided by the Open Science Grid consortium for their support. This work was supported in part by the Offices of NP and HEP within the US DOE Office of Science, the US NSF, the Sloan Foundation, the DFG cluster of excellence 'Origin and Structure of the Universe', CNRS/IN2P3, RA, RPL, and EMN of France, STFC and EPSRC of the United Kingdom, FAPESP of Brazil, the Russian Ministry of Sci. and Tech., the NNSFC, CAS, MoST, and MoE of China, IRP and GA of the Czech Republic, FOM of the Netherlands, DAE, DST, and CSIR of the Government of India, the Polish State Committee for Scientific Research, and the Korea Sci. & Eng. Foundation and Korea Research Foundation.

[1] J. Adams *et al.* (STAR Collaboration), Nucl. Phys. **A757**, 102 (2005).
[2] A. Andronic, P. Braun-Munzinger, and J. Stachel, Nucl. Phys. **A772**, 167 (2006); J. Cleymans and K. Redlich, Phys. Rev. C **60**, 054908 (1999); F. Becattini, J. Manninen, and M. Gazdzicki, *ibid.* **73**, 044905 (2006).
[3] E. Laerman and O. Philipsen, Annu. Rev. Nucl. Part. Sci. **53**, 163 (2003); K. Rajagopal and F. Wilczek, arXiv:hep-ph/0011333; M. A. Stephanov, in *CPODLAT2006 Proceedings*, PoS(LAT2006)024 (SISSA, Trieste, Italy, 2006).
[4] J. Adams *et al.* (STAR Collaboration), Phys. Rev. Lett. **91**, 072304 (2003); **91**, 172302 (2003); B. I. Abelev *et al.* (STAR Collaboration), *ibid.* **97**, 152301 (2006); Phys. Lett. **B655**, 104 (2007); S. S. Adler *et al.* (PHENIX Collaboration), Phys. Rev. Lett. **91**, 072301 (2003).
[5] B. I. Abelev *et al.* (STAR Collaboration), Phys. Rev. Lett. **99**, 112301 (2007); Phys. Rev. C **77**, 054901 (2008).
[6] Y. Aoki *et al.*, Nature (London) **443**, 675 (2006); M. Cheng *et al.*, Phys. Rev. D **77**, 014511 (2008).
[7] S. Ejiri, Phys. Rev. D **78**, 074507 (2008).
[8] M. Asakawa and K. Yazaki, Nucl. Phys. **A504**, 668 (1989); A. Barducci *et al.*, Phys. Lett. **B231**, 463 (1989); Phys. Rev. D **41**, 1610 (1990); M. A. Stephanov, Int. J. Mod. Phys. A **20**, 4387 (2005).
[9] R. V. Gavai and S. Gupta, Phys. Rev. D **78**, 114503 (2008); Z. Fodor and S. D. Katz, J. High Energy Phys. 04 (2004) 050.
[10] B. Mohanty, Nucl. Phys. **A830**, 899c (2009).
[11] M. A. Stephanov, K. Rajagopal, and E. V. Shuryak, Phys. Rev. Lett. **81**, 4816 (1998); Y. Hatta and M. A. Stephanov, *ibid.* **91**, 102003 (2003); M. A. Stephanov, *ibid.* **102**, 032301 (2009); F. Karsch, D. Kharzeev, and K. Tuchin, Phys. Lett. **B663**, 217 (2008).
[12] B. I. Abelev *et al.* (STAR Collaboration), STAR Internal Note SN0493, 2009 (unpublished).
[13] T. Satogata *et al.*, in *CPOD2007 Proceedings*, PoS(CPOD2007)051 (SISSA, Trieste, Italy, 2007).
[14] K. H. Ackermann *et al.*, Nucl. Instrum. Methods A **499**, 624 (2003).
[15] W. J. Llope *et al.*, Nucl. Instrum. Methods A **522**, 252 (2004).
[16] M. Anderson *et al.*, Nucl. Instrum. Methods A **499**, 659 (2003).
[17] K. H. Ackermann *et al.*, Nucl. Instrum. Methods A **499**, 713 (2003).
[18] D. Kharzeev and M. Nardi, Phys. Lett. **B507**, 121 (2001).
[19] C. Amsler *et al.*, Phys. Lett. **B667**, 1 (2008).
[20] B. B. Back *et al.* (PHOBOS Collaboration), Phys. Rev. C **70**, 021902 (2004).
[21] H. Bichsel, Nucl. Instrum. Methods A **562**, 154 (2006); S. Eidelman *et al.* (Particle Data Group), Phys. Lett. **B592**, 1 (2004); in Proceedings of the 8th International Conference on Advance Technology and Particle Physics, (ICATPP), Como, Italy, 6–10, Oct. 2003 (unpublished), p. 448.
[22] M. Shao *et al.*, Nucl. Instrum. Methods A **558**, 419 (2006); Y. Xu *et al.*, arXiv:0807.4303 [physics.ins-det].
[23] B. I. Abelev *et al.* (STAR Collaboration), Phys. Rev. C **79**, 034909 (2009).
[24] A. M. Poskanzer and S. A. Voloshin, Phys. Rev. C **58**, 1671 (1998).
[25] J. Adams *et al.* (STAR Collaboration), Phys. Rev. C **72**, 014904 (2005).
[26] G. I. Kopylov and M. I. Podgoretsky, Sov. J. Nucl. Phys. **15**, 219 (1972) [Yad. Fiz. **15**, 392 (1972)].
[27] U. W. Heinz and B. V. Jacak, Annu. Rev. Nucl. Part. Sci. **49**, 529 (1999).
[28] G. Bertsch, M. Gong, and M. Tohyama, Phys. Rev. C **37**, 1896 (1988).
[29] S. Pratt, Phys. Rev. D **33**, 1314 (1986).
[30] S. Chapman, P. Scotto, and U. W. Heinz, Phys. Rev. Lett. **74**, 4400 (1995).
[31] B. I. Abelev *et al.* (STAR Collaboration), Phys. Rev. C **80**, 024905 (2009).
[32] J. Adams *et al.* (STAR Collaboration), Phys. Rev. C **71**, 044906 (2005).
[33] M. A. Lisa, S. Pratt, R. Soltz, and U. Wiedemann, Annu. Rev. Nucl. Part. Sci. **55**, 357 (2005).
[34] M. G. Bowler, Phys. Lett. **B270**, 69 (1991); Yu. Sinyukov, R. Lednický, S. V. Akkelin, J. Pluta, and B. Erazmus, *ibid.* **B432**, 248 (1998); R. Lednicky, arXiv:nucl-th/0212089.
[35] V. Fine and P. Nevski, in *Proceedings of CHEP-2000*, Padova, Italy, p. 143.
[36] J. Adams *et al.* (STAR Collaboration), Phys. Rev. C **70**, 041901 (2004).
[37] J. Adams *et al.* (STAR Collaboration), Phys. Rev. Lett. **92**, 112301 (2004).
[38] L. Ahle *et al.* (E866 Collaboration and E917 Collaboration), Phys. Lett. **B490**, 53 (2000); L. Ahle *et al.* (E866 Collaboration and E917 Collaboration), *ibid.* **B476**, 1 (2000); J. L. Klay *et al.* (E895 Collaboration), Phys. Rev. Lett. **88**, 102301 (2002); J. Barrette *et al.* (E877 Collaboration), Phys. Rev. C **62**, 024901 (2000); Y. Akiba *et al.* (E802 Collaboration), Nucl. Phys. **A610**, 139c (1996); L. Ahle *et al.* (E802 Collaboration), Phys. Rev. C **60**, 064901 (1999); **60**, 044904 (1999); **57**, R466 (1998).
[39] S. V. Afanasiev *et al.* (NA49 Collaboration), Phys. Rev. C **66**, 054902 (2002); C. Alt *et al.* (NA49 Collaboration), *ibid.* **77**,

024903 (2008); **73**, 044910 (2006); T. Anticic *et al.* (NA49 Collaboration), *ibid.* **69**, 024902 (2004).
[40] S. S. Adler *et al.* (PHENIX Collaboration), Phys. Rev. C **71**, 034908 (2005).
[41] L. Van Hove, Phys. Lett. **B118**, 138 (1982).
[42] B. Mohanty, J. Alam, S. Sarkar, T. K. Nayak, and B. K. Nandi, Phys. Rev. C **68**, 021901(R) (2003), and references therein.
[43] S. Chatterjee, R. M. Godbole, and S. Gupta, arXiv:0906.2523v1 [hep-ph]; A. Andronic, P. Braun-Munzinger, and J. Stachel, Phys. Lett. **B673**, 142 (2009); J. K. Nayak, J. Alam, P. Roy, A. K. Dutt-Mazumder, and B. Mohanty, Acta Phys. Slov. **56**, 27 (2006); B. Tomasik and E. E. Kolomeitsev, Eur. Phys. J. C **49**, 115 (2007); J. Cleymans, H. Oeschler, K. Redlich, and S. Wheaton, Eur. Phys. J. A **29**, 119 (2006); J. Rafelski, I. Kuznetsova, and J. Letessier, J. Phys. G **35**, 044011 (2008).
[44] A. H. Tang, J. Phys. G **34**, S277 (2007).
[45] R. J. M. Snellings, H. Sorge, S. A. Voloshin, F. Q. Wang, and N. Xu, Phys. Rev. Lett. **84**, 2803 (2000); J. Brachmann *et al.*, Phys. Rev. C **61**, 024909 (2000); L. P. Csernai and D. Rohrich, Phys. Lett. **B458**, 454 (1999); H. Stoecker, Nucl. Phys. **A750**, 121 (2005).
[46] B. B. Back *et al.* (PHOBOS Collaboration), Phys. Rev. C **72**, 051901 (2005).
[47] B. B. Back *et al.* (PHOBOS Collaboration), Phys. Rev. Lett. **94**, 122303 (2005).
[48] C. Adler *et al.* (STAR Collaboration), Phys. Rev. C **66**, 034904 (2002).
[49] J. Adams *et al.* (STAR Collaboration), Phys. Rev. Lett. **93**, 252301 (2004).
[50] B. B. Back *et al.* (PHOBOS Collaboration), Phys. Rev. Lett. **89**, 222301 (2002).
[51] S. S. Adler *et al.* (PHENIX Collaboration), Phys. Rev. Lett. **91**, 182301 (2003).
[52] S. S. Adler *et al.* (PHENIX Collaboration), Phys. Rev. Lett. **94**, 232302 (2005).
[53] B. I. Abelev *et al.* (STAR Collaboration), Phys. Rev. Lett. **101**, 252301 (2008).
[54] C. Alt *et al.* (NA49 Collaboration), Phys. Rev. C **68**, 034903 (2003).
[55] B. I. Abelev *et al.* (STAR Collaboration), Phys. Rev. C **75**, 054906 (2007).
[56] J. Barrette *et al.* (E877 Collaboration), Phys. Rev. C **55**, 1420 (1997).
[57] A. Adare *et al.* (PHENIX Collaboration), Phys. Rev. Lett. **98**, 162301 (2007).
[58] B. Alver *et al.* (PHOBOS Collaboration), Phys. Rev. Lett. **98**, 242302 (2007).
[59] G. Goldhaber, S. Goldhaber, W. Y. Lee, and A. Pais, Phys. Rev. **120**, 300 (1960).
[60] E. Schnedermann, J. Sollfrank, and U. Heinz, Phys. Rev. C **48**, 2462 (1993).
[61] P. Braun-Munzinger, I. Heppe, and J. Stachel, Phys. Lett. **B465**, 15 (1999).
[62] J. Cleymans, H. Oeschler, K. Redlich, and S. Wheaton, Phys. Rev. C **73**, 034905 (2006); F. Becattini, J. Manninen, and M. Gazdzicki, *ibid.* **73**, 044905 (2006); A. Andronic, P. Braun-Munzinger, and J. Stachel, Nucl. Phys. **A772**, 167 (2006).
[63] R. Chatterjee, D. K. Srivastava, and S. Jeon, Phys. Rev. C **79**, 034906 (2009); P. Huovinen, P. V. Ruuskanen, and S. S. Rasanen, Phys. Lett. **B535**, 109 (2002); A. K. Chaudhuri, J. Phys. G **29**, 235 (2003); J. Alam, S. Sarkar, T. Hatsuda, T. K. Nayak, and B. Sinha, Phys. Rev. C **63**, 021901 (2001); D. d'Enterria and D. Peressounko, Eur. Phys. J. C **46**, 451 (2006); J. Alam *et al.*, J. Phys. G **34**, 871 (2007).
[64] A. Adare *et al.* (PHENIX Collaboration), arXiv:0804.4168 [nucl-ex].
[65] M. M. Aggarwal *et al.* (WA98 Collaboration), Phys. Rev. Lett. **85**, 3595 (2000).
[66] Y. Aoki *et al.*, Phys. Lett. **B643**, 46 (2006); M. Cheng *et al.*, Phys. Rev. D **74**, 054507 (2006).
[67] B. Bonner *et al.*, Nucl. Instrum. Methods A **508**, 181 (2003); M. Shao *et al.*, *ibid.* **492**, 344 (2002); J. Wu *et al.*, *ibid.* **538**, 243 (2005); J. Adams *et al.* (STAR Collaboration), Phys. Lett. **B616**, 8 (2005).